Accuracy and efficiency in computing electrostatic potential for an ion channel model in layered dielectric/electrolyte media

Huimin Lin [a] Huazhong Tang [a] Wei Cai [b]

[a]*HEDPS, CAPT & LMAM, School of Mathematical Sciences, Peking University, Beijing 100871, China*

[b]*Department of Mathematics and Statistics, University of North Carolina at Charlotte, Charlotte, NC 28223, USA*

Suggested Running Head:

Accuracy and efficiency in computing electrostatic potential for an ion channel model

Corresponding Author:

Prof. Wei Cai

Department of Mathematics and Statistics,

University of North Carolina at Charlotte,

Charlotte, NC 28223-0001

Phone: 704-687-4581, Fax: 704-687-6415,

Email: wcai@uncc.edu

Abstract

This paper will investigate the numerical accuracy and efficiency in computing the electrostatic potential for a finite-height cylinder, used in an explicit/implicit hybrid solvation model for ion channel and embedded in a layered dielectric/electrolyte medium representing a biological membrane and ionic solvents. A charge locating inside the cylinder cavity, where ion channel proteins and ions are given explicit atomistic representations, will be influenced by the polarization field of the surrounding implicit dielectric/electrolyte medium. Two numerical techniques, a specially designed boundary integral equation method and an image charge method, will be investigated and compared in terms of accuracy and efficiency for computing the electrostatic potential. The boundary integral equation method based on the three-dimensional layered Green's functions provides a highly accurate solution suitable for producing a benchmark reference solution, while the image charge method is found to give reasonable accuracy and highly efficient and viable to use the fast multipole method for interactions of a large number of charges in the atomistic region of the hybrid solvation model.

Key words: Poisson-Boltzmann equation, layered electrolytes and dielectrics, image charge method, ion channels, the explicit/implicit hybrid solvation model

1. Introduction

Ion channels play a key role in many biological processes, including cell-cell communication, signaling, muscle contraction etc. And it is well known that the electrostatic interaction is important in the selectivity and transport of ions through biological ion channels. The description of the membrane/solvents around an ion channel can be either atomistic as in an explicit model or continuum as in an implicit model. The selection of a specific model for the solvent depends on the accuracy and efficiency desired for the overall simulation. In order to take advantage of the accuracy of the explicit model and the efficiency of the implicit model, the explicit/implicit hybrid solvation model has been actively studied [1–7]. In such a model, the simulation system is partitioned into two regions, the inner region, usually of a regular geometric shape such as a finite cylinder in this study, containing passing ions and transmembrane channel proteins, and the remaining outer region exterior to the cylinder. In the former region, an atomistic description is used for the ion channel proteins and transgressing ions, while in the latter region, the membrane and solvents are described by dielectric constants or Debye-Hückel length parameters modeling the solvents' conductivity and concentrations. In molecular dynamics simulations using a hybrid solvation model, only the atoms inside the explicit region are dynamically simulated while the effect of the implicit region is included by the use of a reaction field, which results from the polarization of the implicit solvents and membrane by charges inside the explicit region. Therefore, for an hybrid solvation model of ion channels it is critical to have a fast and accurate method to calculate the reaction field for a finite-height cylinder embedded in a layered dielectric/electrolyte medium for ion channel simulations in atomic details.

Due to the complicated and infinite inhomogeneous setting of the hybrid solvation model, it is a computational challenge to find an accurate and fast

numerical method for the reaction field of the implicit region. Traditional finite difference or finite element methods have been used to solve the Poisson equation for the reaction field; however, issues such as artificial boundary conditions for the truncated computational domain and the interface treatment for the membrane and ion-channel walls have not been resolved completely. Previous work treating dielectric interfaces for ion-channels includes computing the polarization surface charges using a variational formulation [21], empirical formulas for self-energies of ions in channels [22], and an asymptotical analytical method [23,24]. A more natural and accurate candidate for handling the infinite region and dielectric boundaries is to use a surface integral equation method applied to the boundary of the finite-height cylinder cavity while the interface conditions along the membrane/solvents are handled by a layered Green's function, which addresses the interface conditions in its definition. Alternatively, the image charge method, as a semi-analytical approach, can also be used to find the reaction field for regular shaped geometries including dielectric spheres [11] and a finite-height cylinder. These two methods will be the subjects of study in this paper.

One of the challenges for high accuracy in surface integral equation method comes from the difficulties caused by the corner/edge singularities of the surface. There have been a large number of special techniques proposed to eliminate the error pollution from the geometry irregularities, including graded meshes and special charge basis [17–20]. However, simply and easily implementable methods are still in demand. This paper will adopt a different approach to circumvent this difficulty for the hybrid solvation model of ion channel by deforming the geometry of the finite-height finite cylinder to a smooth semi-sphere top cylinder. Then, by using layered Green's functions for the layered media inside and outside the new extended geometry, we can remove the singularity effect arising from the geometric edges. The resulting surface integral equation method can be used as a universal benchmark method for

validating other types of numerical solutions including the finite difference and finite element methods. With the specially formed surface integral equation method, we are also in a position to carefully study a previously proposed image charge method for finding the reaction field for the finite-height cylinder [43]. Comparison and validation of the image charge method will be conducted.

The rest of the paper is organized as follows. In Section 2, the background material on the hybrid solvation model for ion channels is given and how the reaction field can be used for molecular dynamics simulation of ion channels would be discussed. Section 3 presents the concept and construction of the layered Green's function for the Poisson and Poisson-Boltzmann equations. Section 4 formulates the surface integral equation method for the electrostatic potential based on an extended geometry for the finite-height cylinder. Section 5 reviews the previous image charge method. In Section 6, numerical tests with both the boundary integral equation method and the image charge method are carried out and compared. Finally, a conclusion is given in Section 7.

2. A hybrid solvation model for ion channels

The hybrid solvation model for ion channels in Fig. 1 consists of a cavity of a finite-height cylinder embedded in a layered dielectric/electrolyte medium representing the biological membrane and ionic solvents. Inside the cylinder, the channel proteins and transgressing ions are treated with explicit atomistic representations while, outside the cylinder, the membrane and solvents are treated as continuous dielectrics. Moreover, the ionic solvents above and below the membrane are modeled by the Debye-Hückel (D-H) mean-field theory for the mobile ion density distributions, which gives the Poisson-Boltzmann (P-B) equation for the electrostatic potential in the electrolyte solvents [25].

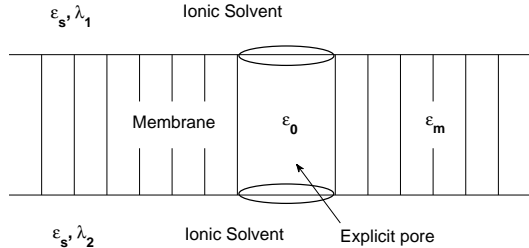As shown in Fig. 1, the dielectric constants in the interior of the cylinder, the

5

Fig. 1. Schematic illustration of an ion-channel hybrid model.

membrane, and the ionic solvent are denoted by ε_0, ε_s, and ε_m, respectively. And λ_1 and λ_2 are the inverse Debye-Hückel lengths of the ionic solvents above and below the membrane, respectively. Now, let us assume that point charges q_i locate at $\mathbf{r}_i$ inside the cylinder. The potential field ϕ satisfies the following P-B equation:

$$\left[\nabla^2\phi(\mathbf{r}) - \lambda^2(\mathbf{r})\phi(\mathbf{r})\right] = -\frac{4\pi}{\varepsilon(\mathbf{r})}\sum_{i=1}^{N} q_i\delta(\mathbf{r} - \mathbf{r}_i). \tag{1}$$

Here, $\varepsilon(\mathbf{r})$ and $\lambda(\mathbf{r})$ are two piecewise constant functions defined by corresponding dielectric constant and the inverse Debye-Hückel length at point $\mathbf{r} = (x, y, z)$, as shown in Fig. 1. If $\mathbf{r}$ is inside the cylinder, we have $\lambda(\mathbf{r}) = 0$, Eq. (1) then reduces to a Poisson equation [32]. Moreover, as the fixed charges q_i are located inside the cylinder, Eq. (1) is a homogeneous Poisson-Boltzmann equation outside the cylinder [42]. On the dielectric interface between different regions in the hybrid solvation model, the potential ϕ and its normal derivative satisfy the following continuity conditions:

$$[\phi(\mathbf{r})] = 0, \qquad [\varepsilon(\mathbf{r})\frac{\partial\phi}{\partial n}(\mathbf{r})] = 0,$$

where $[\,\cdot\,]$ denotes the jump across an interface.

The solution to (1) is decomposed into two parts, a direct Coulombic potential due to the charge in a homogeneous medium of the property of the dielectric cylindrical cavity and a second part, so-called reaction field $\phi_{\mathrm{rf}}(\mathbf{r})$, which re-

flects the polarization of the dielectric medium outside the cylinder. Namely, we have the following decomposition

$$\phi(\mathbf{r}) = \frac{1}{\varepsilon_0} \sum_{i=1}^{N} \frac{q_i}{|\mathbf{r} - \mathbf{r}_i|} + \phi_{\mathrm{rf}}(\mathbf{r}). \tag{2}$$

The main issues for obtaining accurate and fast numerical solution to (1) consist of treating the material inhomogeneities in the hybrid solvation model and the singular behavior of the potential caused by the presence of the fixed point charges q_i. Two numerical methods are ideal for handling these issues, one is the boundary integral equation using layered Green's functions where the boundary conditions along layer interfaces are built into the definitions of the Green's functions. The other is the image method where the interface conditions on the layer and cylinder interfaces can be handled by introducing appropriate image charges. Each of these two methods will have its own advantages in terms of accuracy and efficiency. While the former will be able to produce highly accurate solutions once the geometric singularity from the edges of the cylinder is taken care of, the image charge method is a semi-analytical and efficient method and leads itself to the fast multipole method implementation for computing the relevant electrostatic interactions of many charges in an atomic system. The accuracy and efficiency of the two methods is our objective in studying numerical approximations to the potential problem (1).

For molecular dynamics simulations of ion channels, once the electrostatic potential is obtained, the electrostatic force on a given charge due to all other charges can be obtained by differentiating the potential functions. Other forces such as the Lennard-Jones or van der Waals forces is short-ranged force and can also be obtained by taking the derivatives of their corresponding potentials. Finally, the Newton's equation of motion is employed to evolve the locations of all charges, and statistical analysis of the trajectories of the charges would then give the macroscopic properties and structure information of the

ion channel system. As the electrostatic interactions are long-ranged, the calculation of the electrostatic potential is the most time consuming part in molecular dynamics simulations, the efficiency and accuracy of a computational method for the electrostatic potential would directly affect the practicality of the simulation methods. Therefore, an efficient method to solve equation (1) is crucial for practical simulations of ion channels in atomistic details.

3. Layered Green's functions

In order to form a boundary integral equation for the hybrid solvation model of ion channel, a 3-D layered Green's function would be needed for the P-B equation (1). Due to the symmetry of the layered media in the horizontal directions, the 2-D Fourier transform can be used to obtain the Fourier spectral form of the Green's function. Moreover, the Hankel transform can be used to reduce the 2-D Fourier spectral form to 1-D Sommerfeld-type integrals.

3.1 Fourier spectral form of the Green's function

$\Omega_1, \varepsilon_1, \lambda_1$

_____ $z=D$

$\Omega_2, \varepsilon_2, \lambda_2$

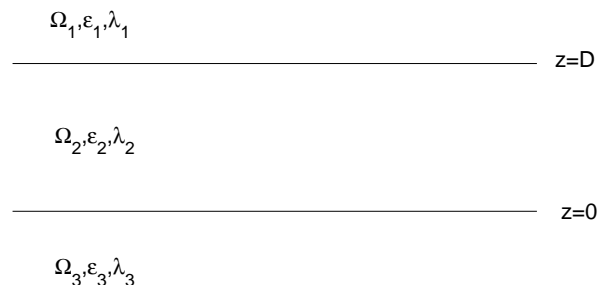_____ $z=0$

$\Omega_3, \varepsilon_3, \lambda_3$

Fig. 2. Schematic illustration of a three-layer structure.

For convenience, we illustrate the technique using a three-layer medium as depicted in Fig. 2, which can be easily extended to any multi-layered medium.

8

In Fig. 2, two interfaces are located at $z = 0$ and $z = D$, respectively, where D is the thickness of the middle layer, and ε_i and λ_i are respectively the dielectric constant and inverse Debye-Hückel lengths for area Ω_i, $i = 1, 2, 3$. The fundamental solution $G(,')$ we concerned satisfies the equation of following form.

$$\varepsilon(\mathbf{r}) \left[\nabla^2 G(\mathbf{r}, \mathbf{r}') - \lambda^2(\mathbf{r}) G(\mathbf{r}, \mathbf{r}') \right] = -\delta(\mathbf{r} - \mathbf{r}'), \tag{3}$$

subject to the continuity conditions across both interfaces

$$[G(\mathbf{r}, \mathbf{r}')]_{z=0,D} = 0, \qquad \left[\varepsilon(\mathbf{r}) \frac{\partial G(\mathbf{r}, \mathbf{r}')}{\partial \mathbf{n}} \right]_{z=0,D} = 0, \tag{4}$$

where $\varepsilon(\mathbf{r}) = \varepsilon_i$, $\lambda(\mathbf{r}) = \lambda_i$ for $\mathbf{r} \in \Omega_i$, $i = 1, 2, 3$.

When $\mathbf{r}' \in \Omega_j$, $j = 1, 2, 3$, let $P_j(\mathbf{r}, \mathbf{r}')$ satisfy the following equation for a homogeneous space with dielectric constant ε_j

$$\varepsilon_j \left[\nabla^2 P_j(\mathbf{r}, \mathbf{r}') - \lambda_j^2 P_j(\mathbf{r}, \mathbf{r}') \right] = -\delta(\mathbf{r} - \mathbf{r}'), \tag{5}$$

whose solution is

$$
\begin{aligned}
P_j(\mathbf{r}, \mathbf{r}') &= \frac{e^{-\lambda_j |\mathbf{r} - \mathbf{r}'|}}{4\pi \varepsilon_j |\mathbf{r} - \mathbf{r}'|} \\
&= \frac{1}{2\pi} \int_{-\infty}^{+\infty} \int_{-\infty}^{+\infty} dk_x dk_y e^{ik_x(x-x')} e^{ik_y(y-y')} \frac{e^{-\tilde{\eta}_j |z-z'|}}{4\pi \varepsilon_j \tilde{\eta}_j},
\end{aligned} \tag{6}
$$

where

$$\tilde{\eta}_j = \sqrt{k_\rho^2 + \lambda_j^2}, \tag{7}$$

and k_x and k_y are the spectral variables for x and y, respectively, $k_\rho = \sqrt{k_x^2 + k_y^2}$.

If defing

$$G_{\mathrm{mod},j}(\mathbf{r}, \mathbf{r}') = \begin{cases} G(\mathbf{r}, \mathbf{r}') - P_j(\mathbf{r}, \mathbf{r}'), & \mathbf{r} \in \Omega_j, \\ \\ G(\mathbf{r}, \mathbf{r}'), & \mathbf{r} \notin \Omega_j, \end{cases} \tag{8}$$

then it is not difficult to see from (3)-(5) that $G_{\mathrm{mod},j}$ satisfies

$$\nabla^2 G_{\mathrm{mod},j}(\mathbf{r}, \mathbf{r}') - \lambda_i^2 G_{\mathrm{mod},j}(\mathbf{r}, \mathbf{r}') = 0, \qquad \mathbf{r} \in \Omega_i, i = 1, 2, 3. \tag{9}$$

Using using 2-D Fourier transform in the x and y directions gives

$$\frac{\partial^2 \hat{G}_{\mathrm{mod},j}}{\partial z^2}(k_\rho, z, z') - \tilde{\eta}_i^2 \hat{G}_{\mathrm{mod},j}(k_\rho, z, z') = 0, \tag{10}$$

whose solution is

$$\hat{G}_{mod,j}(k_\rho, z, z') = \mathrm{Cof}_{i1} e^{-\tilde{\eta}_i z} + \mathrm{Cof}_{i2} e^{\tilde{\eta}_i z}.$$

Using corresponding inverse Fourier transform yields $G_{\mathrm{mod},j}$

$$
\begin{aligned}
&G_{\mathrm{mod},j}(\mathbf{r}, \mathbf{r}') \\
&= \frac{1}{2\pi} \int_{-\infty}^{+\infty} \int_{-\infty}^{+\infty} dk_x dk_y e^{ik_x(x-x')} e^{ik_y(y-y')} \hat{G}_{mod,j}(k_\rho, z, z') \\
&= \frac{1}{2\pi} \int_{-\infty}^{+\infty} \int_{-\infty}^{+\infty} dk_x dk_y e^{ik_x(x-x')} e^{ik_y(y-y')} \left[\mathrm{Cof}_{i1} e^{-\tilde{\eta}_i z} + \mathrm{Cof}_{i2} e^{\tilde{\eta}_i z} \right], \quad \mathbf{r} \in \Omega_i.
\end{aligned}
\tag{11}
$$

Combining it with the definition of $G_{\mathrm{mod},j}(\mathbf{r}, \mathbf{r}')$ in (8) leads to the Fourier spectral form of the 3-D layered Green's function $G(\mathbf{r}, \mathbf{r}')$, see (A.1)-(A.3) in Appendix A. Moreover, the coefficients Cof_{i1} and Cof_{i2} can be found by substituting (6), (8), and (11) into the interface conditions.

3.2   Calculation of the Fourier spectral form of layered Green's function

This section is to discuss the calculation of the Fourier spectral form of the layered Green's function given in the last section through the Hankel transform.

In order to simplify the 2-D integrals in the Fourier spectral form of the Green's function, for a 2-D radial symmetric function, we introduce the polar coordinates in the physical space and the spectral space respectively as follows

$$x - x' = \rho \cos \alpha, \qquad y - y' = \rho \sin \alpha, \tag{12}$$

and

$$k_x = k_\rho \cos \beta, \qquad k_y = k_\rho \sin \beta. \tag{13}$$

Then the 2-D inverse Fourier transform can be rewritten into an 1-D Sommerfeld integral as follows

$$
\begin{aligned}
f(\rho, z, z') &= \mathcal{F}^{-1}\left\{\hat{f}(k_\rho, z, z')\right\} \\
&= \frac{1}{2\pi}\int_{-\infty}^{+\infty}\int_{-\infty}^{+\infty} dk_x dk_y \hat{f}(k_\rho, z, z') e^{i[k_x(x-x')+k_y(y-y')]} \\
&= \frac{1}{2\pi}\int_0^{+\infty} dk_\rho \int_0^{2\pi} d\beta \hat{f}(k_\rho, z, z') k_\rho e^{ik_\rho\rho\cos(\alpha-\beta)} \\
&= \int_0^{+\infty} dk_\rho \hat{f}(k_\rho, z, z') k_\rho J_0(k_\rho\rho),
\end{aligned}
\tag{14}
$$

where $J_0(z)$ is the Bessel function of order 0

$$
J_0(z) = \frac{1}{2\pi}\int_0^{2\pi} e^{iz\sin\theta} d\theta.
$$

The Green's function given by (A.1)-(A.3) in Appendix A can be written into the form of (14) for corresponding specific integrand $\hat{f}$.

To compute the normal derivative of the Green's function, $\frac{\partial G}{\partial \mathbf{n}}$, needed in the coming boundary integral equation, we may first calculate the derivatives $\frac{\partial G}{\partial x}$, $\frac{\partial G}{\partial y}$ and $\frac{\partial G}{\partial z}$ via the following procedure.

From (14), we have

$$
\frac{\partial}{\partial z} f(x, y, z, z') = \int_0^{+\infty} dk_\rho \left[\frac{\partial}{\partial z}\hat{f}(k_\rho, z, z')\, k_\rho J_0(k_\rho\rho)\right].
\tag{15}
$$

Taking $\hat{f}$ as A_i, B_i, C_i, D_i listed Appendix A, leats to

$$
\frac{\partial}{\partial z} A_i(k_\rho, z, z') = -\tilde{\eta}_1 A_i(k_\rho, z, z'), \quad \frac{\partial}{\partial z} B_i(k_\rho, z, z') = -\tilde{\eta}_2 B_i(k_\rho, z, z'),
$$

$$
\frac{\partial}{\partial z} C_i(k_\rho, z, z') = \tilde{\eta}_2 C_i(k_\rho, z, z'), \quad \frac{\partial}{\partial z} D_i(k_\rho, z, z') = \tilde{\eta}_3 D_i(k_\rho, z, z'), \quad i = 1, 2, 3.
$$

On the other hand, in order to calculate the derivatives of the Green's function G in the x- and y-directions, using the identities

$$
\frac{\partial}{\partial x} = \cos\alpha\frac{\partial}{\partial\rho} - \frac{\sin\alpha}{\rho}\frac{\partial}{\partial\alpha}, \qquad \frac{\partial}{\partial y} = \sin\alpha\frac{\partial}{\partial\rho} + \frac{\cos\alpha}{\rho}\frac{\partial}{\partial\alpha},
\tag{16}
$$

11

we obtain

$$
\begin{aligned}
\frac{\partial}{\partial x} f(\rho, z, z') &= \frac{\partial}{\partial x} \mathcal{F}^{-1}\left\{\hat{f}(k_\rho, z, z')\right\} \\
&= \left\{\cos\alpha \frac{\partial}{\partial\rho} - \frac{\sin\alpha}{\rho}\frac{\partial}{\partial\alpha}\right\} \mathcal{F}^{-1}\left\{\hat{f}(k_\rho, z, z')\right\} \\
&= \cos\alpha \int_0^{+\infty} dk_\rho \hat{f}(k_\rho, z, z') k_\rho \frac{\partial}{\partial\rho} J_0(k_\rho\rho) \\
&= -\cos\alpha \int_0^{+\infty} dk_\rho \hat{f}(k_\rho, z, z') k_\rho^2 \, J_1(k_\rho\rho),
\end{aligned}
\tag{17}
$$

and

$$
\frac{\partial}{\partial y} f(\rho, z, z') = -\sin\alpha \int_0^{+\infty} dk_\rho \hat{f}(k_\rho, z, z') k_\rho^2 \, J_1(k_\rho\rho),
\tag{18}
$$

where the identity $J_0'(\rho) = -J_1(\rho)$ has been used in the last equality, and $J_1(\rho)$ is the Bessel function of order 1 defined by

$$
J_1(z) = \frac{1}{2\pi}\int_0^{2\pi} e^{-i(\theta - z\sin\theta)} d\theta.
$$

Hence, the 3-D layered Green's function and its derivatives can be obtained by numerical quadrature of the 1-D Sommerfeld-type integrals.

4.   Boundary integral equation method for a finite-height cylinder

This section will give a specially designed boundary integral equation for the hybrid solvation model for ion channels and aim to remove the effect of geometric singularities arising from the edges of the finite-height cylinder. The idea is to attach respectively two "virtual" semi-spheres at the top and bottom surfaces of the finite-height cylinder shown in Fig. 1 to form a round-top cylinder, see its schematic illustration in Fig. 3, and then formulate a boundary integral equation on the surface of the resulting round-top cylinder, instead. The round-top cylinder has layered medium both inside and outside, thus the layered Green's functions for the interior and exterior layered medium may be used to derive the boundary integral equation. It should be emphasized
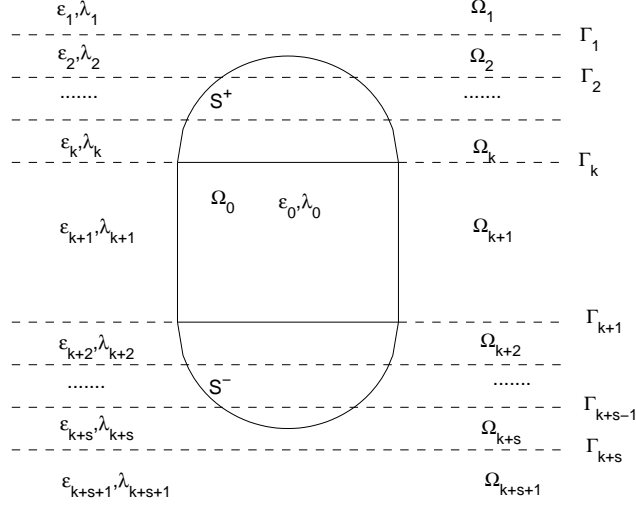
Fig. 3. Schematic illustration of a round-top cylinder.

that the "virtual" semi-spherical surfaces are only used for the mathematical formulation and do not alter the physical dielectric properties of the medium where they are embedded into.

4.1 The boundary integral equations

Let Ω_0 denote the finite-height cylinder with disk top and bottom, S^+ and S^- be two semi-spheres attached to the disk top and bottom of the finite-height cylinder, and $\Omega^* = \Omega_0 \cup S^+ \cup S^-$ be the round-top cylinder. For the layered structure as shown in Fig. 3, the sub-region Ω_i is characterized by dielectric constant ε_i and inverse Debye-Hückel length λ_i and the piecewise constant functions $\varepsilon(\mathbf{r})$ and $\lambda(\mathbf{r})$ in (1) become

$$(\varepsilon(\mathbf{r}), \lambda(\mathbf{r})) = \begin{cases} (\varepsilon_0, \lambda_0 = 0), \ \mathbf{r} \in \Omega_0, \\ (\varepsilon_{k+1}, \lambda_{k+1}), \ \mathbf{r} \in \Omega_{k+1}/\Omega_0, \\ (\varepsilon_j, \lambda_j), \qquad \mathbf{r} \in \Omega_j, j = 1, 2, \cdots, k, k+2, k+3, \cdots, k+s+1. \end{cases}$$

(19)

13

Before deriving our boundary integral equations (BIE), we first list some additional notations and illustrations here for later reference:

- Γ_i is the interface between two adjacent layers, and the normal vector $\mathbf{n}_i$ on Γ_i is defined as the region Ω_i's outward normal vector on the boundary Γ_i, i.e., $\mathbf{n}_i$ directs into Ω_{i+1}, $i = 1, 2, \cdots, k+s$

- Γ_i will be separated into two parts: inside and outside Ω^*, denoted by $\Gamma_i^+ = \Gamma_i \cap (\Omega^*)^c$ and $\Gamma_i^- = \Gamma_i \cap \Omega^*$, respectively, where $(\Omega^*)^c =^3 /\Omega^*$.

- The surface of the finite-height cylinder is denoted by $\partial \Omega_0 = \partial \Omega_0^u \cup \partial \Omega_0^s \cup \partial \Omega_0^d$, i.e. a union of corresponding top, side, and bottom surfaces, and the normal vector on each surface is defined directing from the inside of the cylinder to the outside.

- Define $P^\pm = \partial S^\pm$ as the surface of the semi-sphere $S^\pm$, and the normal vector on $P^\pm$ are directing from the inside of the semi-sphere to the outside.

- Denote $\phi(\mathbf{r}) = \phi_i(\mathbf{r})$ for $\mathbf{r} \in \Omega_i$, $i = 0, 1, 2, \cdots, k+s+1$, where the potential $\phi_i(\mathbf{r})$ is a smooth function defined in the subregion Ω_i. Note that the jumps $[\phi]$ and $[\varepsilon \frac{\partial \phi}{\partial \mathbf{n}}]$ are equal to zero at each interface Γ_i and $\partial \Omega_0$.

In a layered medium depicted in Fig.4 with a piecewise layered dielectric properties, same as those outside the round-top cylinder Ω^*,

$$\bar{\lambda}(\mathbf{r}) = \lambda_i, \ \ \bar{\varepsilon}(\mathbf{r}) = \varepsilon_i, \ \ i = 1, 2, \cdots, k+s+1, \tag{20}$$

the fundamental solution $\bar{G}(\mathbf{r}, \mathbf{r}')$ of Eq. (1) with the singularity at $\mathbf{r}'$ satisfies

$$\bar{\varepsilon}(\mathbf{r}) \left[\nabla^2 \bar{G}(\mathbf{r}, \mathbf{r}') - \bar{\lambda}^2(\mathbf{r}) \bar{G}(\mathbf{r}, \mathbf{r}') \right] = -\delta(\mathbf{r} - \mathbf{r}'), \tag{21}$$

and the interface conditions

$$[\bar{G}(\mathbf{r}, \mathbf{r}')] = 0, \ \ \left[\bar{\varepsilon}(\mathbf{r}) \frac{\partial \bar{G}}{\partial \mathbf{n}}(\mathbf{r}, \mathbf{r}') \right] = 0, \ \ \mathbf{r} \in \Gamma_i, \ i = 1, 2, \cdots, k+s,$$

where

$$\bar{G}(\mathbf{r}, \mathbf{r}') = \bar{G}_i(\mathbf{r}, \mathbf{r}'), \ \ \ \ \mathbf{r} \in \Omega_i.$$
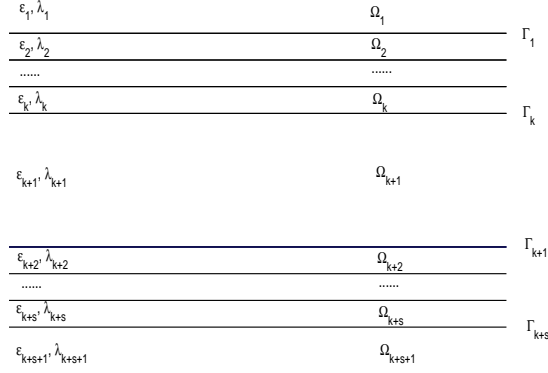
Fig. 4. Schematic illustration of a layered media, same as that outside the round-top cylinder Ω^*.

Multiplying Eq.(1) by $\bar{\varepsilon}(\mathbf{r})\bar{G}(\mathbf{r}, \mathbf{r}')$ and Eq.(21) by $\phi(\mathbf{r})$ and then integrating their difference on $\mathbb{R}^3 \backslash (\Omega^* \cup B(\mathbf{r}', \rho))^c$ yields

$$
\begin{aligned}
0 &= \int_{\mathbb{R}^3 \backslash (\Omega^* \cup B(\mathbf{r}', \rho))} \bar{\varepsilon}(\mathbf{r}) \left[\bar{G}(\mathbf{r}, \mathbf{r}') \nabla^2 \phi(\mathbf{r}) - \phi(\mathbf{r}) \nabla^2 \bar{G}(\mathbf{r}, \mathbf{r}') \right] d\mathbf{r} \\
&= \int_{\mathbb{R}^3 \backslash (\Omega^* \cup B(\mathbf{r}', \rho))} \bar{\varepsilon}(\mathbf{r}) \nabla \left[\bar{G}(\mathbf{r}, \mathbf{r}') \nabla \phi(\mathbf{r}) - \phi(\mathbf{r}) \nabla \bar{G}(\mathbf{r}, \mathbf{r}') \right] d\mathbf{r}, \qquad (22)
\end{aligned}
$$

where $B(\mathbf{r}', \rho)$ denotes the small ball centered at $\mathbf{r}'$ with a radius ρ, $0 < \rho \ll 1$. Using the Green's second identity may further give the following integral equation

$$
\begin{aligned}
\phi(\mathbf{r}') &= \int_{\partial \Omega_0^s} \varepsilon_{k+1} \left[\phi_{k+1}(\mathbf{r}) \frac{\partial \bar{G}_{k+1}}{\partial \mathbf{n}}(\mathbf{r}, \mathbf{r}') - \bar{G}_{k+1}(\mathbf{r}, \mathbf{r}') \frac{\partial \phi_{k+1}}{\partial \mathbf{n}}(\mathbf{r}) \right] dS(\mathbf{r}) \\
&\quad + \int_{P^+ \cup P^-} \bar{\varepsilon}(\mathbf{r}) \left[\phi(\mathbf{r}) \frac{\partial \bar{G}}{\partial \mathbf{n}}(\mathbf{r}, \mathbf{r}') - \bar{G}(\mathbf{r}, \mathbf{r}') \frac{\partial \phi}{\partial \mathbf{n}}(\mathbf{r}) \right] dS(\mathbf{r}), \ \mathbf{r}' \in (\Omega^*)^c.
\end{aligned}
$$
$$(23)$$

We refer the readers to Appendix B for its detailed derivations. Let $\mathbf{r}'$ tend to the point $\mathbf{p} \in \partial \Omega_0^s \cup P^+ \cup P^-$ from the outside of Ω^*, then Eq.(23) gives

$$
\begin{aligned}
\frac{1}{2} \phi(\mathbf{p}) &= \int_{\partial \Omega_0^s} \varepsilon_{k+1} \phi_0(\mathbf{r}) \frac{\partial \bar{G}_{k+1}}{\partial \mathbf{n}}(\mathbf{r}, \mathbf{p}) - \varepsilon_0 \bar{G}_{k+1}(\mathbf{r}, \mathbf{p}) \frac{\partial \phi_0}{\partial \mathbf{n}}(\mathbf{r}) dS(\mathbf{r}) \\
&\quad + \int_{P^+ \cup P^-} \bar{\varepsilon}(\mathbf{r}) \left[\phi(\mathbf{r}) \frac{\partial \bar{G}}{\partial \mathbf{n}}(\mathbf{r}, \mathbf{p}) - \bar{G}(\mathbf{r}, \mathbf{p}) \frac{\partial \phi}{\partial \mathbf{n}}(\mathbf{r}) \right] dS(\mathbf{r}), \qquad (24)
\end{aligned}
$$

15

here we have used the interface conditions that

$$\phi_0(\mathbf{p}) = \phi_{k+1}(\mathbf{p}), \quad \varepsilon_0 \frac{\partial \phi_0}{\partial \mathbf{n}}(\mathbf{p}) = \varepsilon_{k+1} \frac{\partial \phi_{k+1}}{\partial \mathbf{n}}(\mathbf{p}), \quad \mathbf{p} \in \partial \Omega_0^s.$$
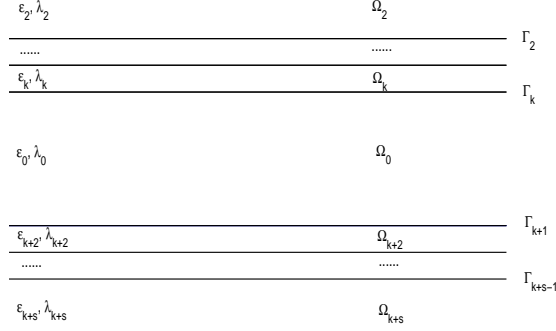
Fig. 5. Schematic illustration of a layered media, same as that inside the round-top cylinder Ω^*.

Similarly, in a layered medium depicted in Fig.5 with a piecewise layered dielectric properties, same as those inside the round-top cylinder, Ω^*

$$(\hat{\varepsilon}(\mathbf{r}), \hat{\lambda}(\mathbf{r})) = \begin{cases} (\varepsilon_i, \lambda_i), \ \mathbf{r} \in \Omega_i, i = 2, 3, \cdots, k, k+2, k+3, \cdots, k+s, \\[2ex] (\varepsilon_0, \lambda_0), \ \mathbf{r} \in \Omega_0, \end{cases} \tag{25}$$

the fundamental solution of Eq. (1) with singularity at $\mathbf{r}'$ satisfies

$$\hat{\varepsilon}(\mathbf{r}) \left[\nabla^2 \hat{G}(\mathbf{r}, \mathbf{r}') - \hat{\lambda}^2(\mathbf{r}) \hat{G}(\mathbf{r}, \mathbf{r}') \right] = -\delta(\mathbf{r} - \mathbf{r}'), \tag{26}$$

and the interface conditions

$$[\hat{G}(\mathbf{r}, \mathbf{r}')] = 0, \quad \left[\hat{\varepsilon}(\mathbf{r}) \frac{\partial \hat{G}}{\partial \mathbf{n}}(\mathbf{r}, \mathbf{r}') \right] = 0, \quad r \in \Gamma_i, i = 2, \cdots, k+s-1,$$

where

$$\hat{G}(\mathbf{r}, \mathbf{r}') = \begin{cases} \hat{G}_0(\mathbf{r}, \mathbf{r}'), \ \mathbf{r} \in \Omega_0, \\[2ex] \hat{G}_i(\mathbf{r}, \mathbf{r}'), \ \mathbf{r} \in \Omega_i, \ i = 2, \cdots, k, k+2, k+3, \cdots, k+s. \end{cases}$$

16

Multiplying Eq.(1) by $\hat{\varepsilon}(\mathbf{r})\hat{G}(\mathbf{r},\mathbf{r}')$ and Eq.(26) by $\phi(\mathbf{r})$ and then integrating their difference on $\Omega^* \backslash B(\mathbf{r}',\rho)$ yields

$$-4\pi\sum_{i=1}^{N} q_i\hat{G}(\mathbf{r}_i,\mathbf{r}') = \int_{\Omega^*\backslash B(\mathbf{r}',\rho)} \hat{\varepsilon}(\mathbf{r})\left[\hat{G}(\mathbf{r},\mathbf{r}')\nabla^2\phi(\mathbf{r}) - \phi(\mathbf{r})\nabla^2\hat{G}(\mathbf{r},\mathbf{r}')\right]d\mathbf{r}$$
$$= \int_{\Omega^*\backslash B(\mathbf{r}',\rho)} \hat{\varepsilon}(\mathbf{r})\nabla\left[\hat{G}(\mathbf{r},\mathbf{r}')\nabla\phi(\mathbf{r}) - \phi(\mathbf{r})\nabla\hat{G}(\mathbf{r},\mathbf{r}')\right]d\mathbf{r}. \quad (27)$$

Using the Green's second identity again, we can get

$$\phi(\mathbf{r}') = \int_{\partial\Omega_0^s} \varepsilon_0 \left[\hat{G}_0(\mathbf{r},\mathbf{r}')\frac{\partial\phi_0}{\partial\mathbf{n}}(\mathbf{r}) - \phi_0(\mathbf{r})\frac{\partial\hat{G}_0}{\partial\mathbf{n}}(\mathbf{r},\mathbf{r}')\right]dS(\mathbf{r})$$
$$+ \int_{P^+\cup P^-} \hat{\varepsilon}(\mathbf{r})\left[\hat{G}(\mathbf{r},\mathbf{r}')\frac{\partial\phi}{\partial\mathbf{n}}(\mathbf{r}) - \phi(\mathbf{r})\frac{\partial\hat{G}}{\partial\mathbf{n}}(\mathbf{r},\mathbf{r}')\right]dS(\mathbf{r})$$
$$+ 4\pi\sum_{i=1}^{N} q_i\hat{G}(\mathbf{r}_i,\mathbf{r}'), \qquad \mathbf{r}' \in \Omega^*, \quad (28)$$

whose detailed derivation has been given in Appendix B.

Let $\mathbf{r}'$ approach to the point $\mathbf{p} \in \partial\Omega_0^s \cup P^+ \cup P^-$ from the inside of Ω^*, then Eq.(28) gives

$$\frac{1}{2}\phi(\mathbf{p}) = \int_{\partial\Omega_0^s} \varepsilon_0 \left[\hat{G}_0(\mathbf{r},\mathbf{p})\frac{\partial\phi_0}{\partial\mathbf{n}}(\mathbf{r}) - \phi_0(\mathbf{r})\frac{\partial\hat{G}_0}{\partial\mathbf{n}}(\mathbf{r},\mathbf{p})\right]dS(\mathbf{r})$$
$$+ \int_{P^+\cup P^-} \hat{\varepsilon}(\mathbf{r})\left[\hat{G}(\mathbf{r},\mathbf{p})\frac{\partial\phi}{\partial\mathbf{n}}(\mathbf{r}) - \phi(\mathbf{r})\frac{\partial\hat{G}}{\partial\mathbf{n}}(\mathbf{r},\mathbf{p})\right]dS(\mathbf{r})$$
$$+ 4\pi\sum_{i=1}^{N} q_i\hat{G}(\mathbf{r}_i,\mathbf{p}). \quad (29)$$

Until now, we have finished the derivation of our boundary integral equations (24) and (29), in which no geometric singularity is involved.

4.2   Finite element approximations for the boundary integral equations

This section is to discuss the finite element approximation of the boundary integral equations (24) and (29). For the sake of convenience, we rewrite the

boundary integral equations (24) and (29) into the following forms

$$\frac{1}{2}f(\mathbf{p}) = \int_{\partial\Omega_0^s} \varepsilon_{k+1}f(\mathbf{r})\frac{\partial\bar{G}_{k+1}}{\partial\mathbf{n}}(\mathbf{r},\mathbf{p}) - \varepsilon_0 h(\mathbf{r})\bar{G}_{k+1}(\mathbf{r},\mathbf{p})dS(\mathbf{r})$$

$$+ \int_{P^+\cup P^-} \bar{\varepsilon}(\mathbf{r})\left[f(\mathbf{r})\frac{\partial\bar{G}}{\partial\mathbf{n}}(\mathbf{r},\mathbf{p}) - h(\mathbf{r})\bar{G}(\mathbf{r},\mathbf{p})\right]dS(\mathbf{r}), \qquad (30)$$

and

$$\frac{1}{2}f(\mathbf{p}) = \int_{\partial\Omega_0^s} \varepsilon_0\left[h(\mathbf{r})\hat{G}_0(\mathbf{r},\mathbf{p}) - f(\mathbf{r})\frac{\partial\hat{G}_0}{\partial\mathbf{n}}(\mathbf{r},\mathbf{p})\right]dS(\mathbf{r})$$

$$+ \int_{P^+\cup P^-} \hat{\varepsilon}(\mathbf{r})\left[h(\mathbf{r})\hat{G}(\mathbf{r},\mathbf{p}) - f(\mathbf{r})\frac{\partial\hat{G}}{\partial\mathbf{n}}(\mathbf{r},\mathbf{p})\right]dS(\mathbf{r})$$

$$+ 4\pi\sum_{i=1}^{N}q_i\hat{G}(\mathbf{r}_i,\mathbf{p}), \qquad (31)$$

where

$$f(\mathbf{r}) = \begin{cases} \phi_0(\mathbf{r}), & \mathbf{r}\in\partial\Omega_0^s, \\ \phi(\mathbf{r}), & \mathbf{r}\in P^+\cup P^-, \end{cases}$$

$$h(\mathbf{r}) = \begin{cases} \frac{\partial\phi_0}{\partial\mathbf{n}}(\mathbf{r}), & \mathbf{r}\in\partial\Omega_0^s, \\ \frac{\partial\phi}{\partial\mathbf{n}}(\mathbf{r}), & \mathbf{r}\in P^+\cup P^-. \end{cases}$$
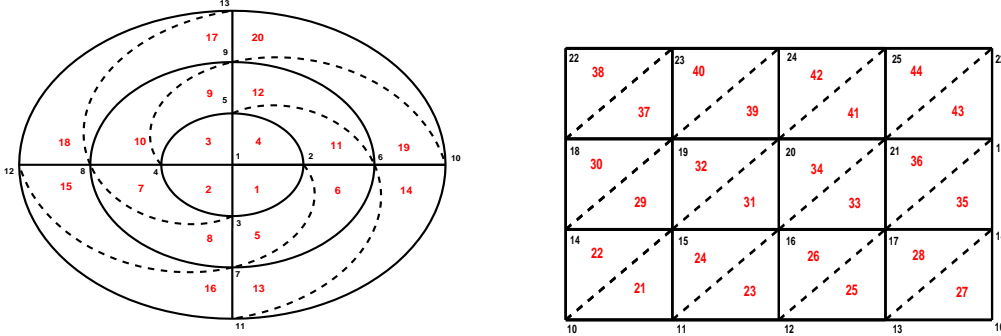

Fig. 6. The planar projection of the body-fitted mesh. Left: top semi-sphere surface; right: the side surface of the cylinder.

A body-fitted mesh is generated for the surface of the round-top cylinder, where each element is set as a curved line triangle of which every point locates exactly on the surface of the round-top cylinder. Fig. 6 shows the planar

18

projection of such body-fitted mesh. Use $\mathbf{r}_t$ to denote the coordinates of the tth mesh vertex, where the index $t \in \{t_1, t_2, \cdots, t_M\}$, and ψ_t be the linear basis function satisfying

$$\psi_{t_i}(\mathbf{r}_{t_j}) = \delta_{ij}.$$

Then the functions $f(\mathbf{r})$ and $h(\mathbf{r})$ can be approximated by

$$f(\mathbf{r}) \approx \sum_t f_t \psi_t(\mathbf{r}), \qquad h(\mathbf{r}) \approx \sum_t h_t \psi_t(\mathbf{r}),$$

where

$$f_t = f(\mathbf{r}_t), \qquad h_t = h(\mathbf{r}_t).$$

Based on the above body-fitted mesh and linear basis function ψ_t, Eqs. (30) and (31) may be approximated as follows

$$
\begin{aligned}
\frac{1}{2}f(\mathbf{p}) = \sum_t f_t &\left[\int_{E_t \cap \partial\Omega_0^s} \varepsilon_{k+1}\psi_t(\mathbf{r})\frac{\partial \bar{G}_{k+1}}{\partial \mathbf{n}}(\mathbf{r},\mathbf{p})dS(\mathbf{r}) \right.\\
&\left. + \int_{E_t \cap (P^+ \cup P^-)} \bar{\varepsilon}(\mathbf{r})\psi_t(\mathbf{r})\frac{\partial \bar{G}}{\partial \mathbf{n}}(\mathbf{r},\mathbf{p})dS(\mathbf{r}) \right]\\
- \sum_t h_t &\left[\int_{E_t \cap \partial\Omega_0^s} \varepsilon_0\psi_t(\mathbf{r})\bar{G}_{k+1}(\mathbf{r},\mathbf{p})dS(\mathbf{r}) \right.\\
&\left. + \int_{E_t \cap (P^+ \cup P^-)} \bar{\varepsilon}(\mathbf{r})\psi_t(\mathbf{r})\bar{G}(\mathbf{r},\mathbf{p})dS(\mathbf{r}) \right]\\
= \sum_t A_{p,t}f_t &- \sum_t B_{p,t}h_t,
\end{aligned}
\tag{32}
$$

and

$$
\begin{aligned}
\frac{1}{2}f(\mathbf{p}) = -\sum_t f_t &\left[\int_{E_t \cap \partial\Omega_0^s} \varepsilon_0\psi_t(\mathbf{r})\frac{\partial \hat{G}_0}{\partial \mathbf{n}}(\mathbf{r},\mathbf{p})dS(\mathbf{r}) \right.\\
&\left. + \int_{E_t \cap (P^+ \cup P^-)} \hat{\varepsilon}(\mathbf{r})\psi_t(\mathbf{r})\frac{\partial \hat{G}}{\partial \mathbf{n}}(\mathbf{r},\mathbf{p})dS(\mathbf{r}) \right]\\
+ \sum_t h_t &\left[\int_{E_t \cap \partial\Omega_0^s} \varepsilon_0\psi_t(\mathbf{r})\hat{G}_0(\mathbf{r},\mathbf{p})dS(\mathbf{r}) \right.\\
&\left. + \int_{E_t \cap (P^+ \cup P^-)} \hat{\varepsilon}(\mathbf{r})\psi_t(\mathbf{r})\hat{G}(\mathbf{r},\mathbf{p})dS(\mathbf{r}) \right]\\
+ 4\pi \sum_{i=1}^N & q_i\hat{G}(\mathbf{r}_i,\mathbf{p})\\
= \sum_t -\tilde{A}_{p,t}f_t &+ \sum_t \tilde{B}_{p,t}h_t + 4\pi\sum_{i=1}^N q_i\hat{G}(\mathbf{r}_i,\mathbf{p}).
\end{aligned}
\tag{33}
$$

where E_t is the set of all elements with the mesh vertex $\mathbf{r}_t$. If letting $\mathbf{p}$ go through all the mesh vertexes $\mathbf{r}_t$, $t = t_1, t_2, \cdots, t_M$, then Eqs. (32)-(33) lead to the finite element approximations of the boundary integral equations (24) and (29) in the following matrix form

$$\begin{bmatrix} \frac{1}{2}I - A & B \\ \frac{1}{2}I + \tilde{A} & -\tilde{B} \end{bmatrix} \begin{bmatrix} \mathbf{f} \\ \mathbf{h} \end{bmatrix} = \begin{bmatrix} \mathbf{0} \\ \mathbf{h} \end{bmatrix}, \tag{34}$$

where the matrices $A = [A_{t_i,t_j}]$, $B = [B_{t_i,t_j}]$, $\tilde{A} = [\tilde{A}_{t_i,t_j}]$ and $\tilde{B} = [\tilde{B}_{t_i,t_j}]$, and the vectors $\mathbf{f} = [f_{t_j}]$, $\mathbf{h} = [h_{t_j}]$ and $\mathbf{b} = [4\pi \sum_{i=1}^{N} q_i \hat{G}(\mathbf{r}_i, \mathbf{r}_{t_j})]$,

As soon as the above linear system (34) is solved, the potential f_t and its derivative h_t are obtained.

In the following, we still need to discuss the evaluation of the singular integrals appeared in (32)-(33) or the elements of the coefficient matrix in (34). A typical term in those singular integrals is taking the following form

$$I = \int_{\triangle_t} F(\mathbf{r}, \mathbf{r}_{t_j}) \psi_t(\mathbf{r}) dS, \tag{35}$$

where $\triangle_t \in E_t$ is a surface element with the mesh vertex $\mathbf{r}_t$, and $F(\mathbf{r}, \mathbf{r}_{t_j})$ is a function with singularity at $\mathbf{r}_{t_j}$, representing $\hat{G}(\mathbf{r}, \mathbf{r}_{t_j})$, $\bar{G}(\mathbf{r}, \mathbf{r}_{t_j})$, $\frac{\partial \hat{G}}{\partial \mathbf{n}}(\mathbf{r}, \mathbf{r}_{t_j})$, or $\frac{\partial \bar{G}}{\partial \mathbf{n}}(\mathbf{r}, \mathbf{r}_{t_j})$.

Let Γ be a conformal transformation from a standard triangular element $\triangle_0$ to the curved triangular element $\triangle_t$, that is to say, the map Γ conforms to geometric shape of the round-top cylinder. The expression of the map Γ is detailedly given in Appendix C. Then, the integral I in (35) can be transforms

into an integral on the element $\triangle_0$ as follows

$$
\begin{aligned}
I &= \int_{\triangle_t} F(\mathbf{r}, \mathbf{r}_{t_j}) \psi_t(\mathbf{r}) dS(\mathbf{r}) \\
&= \int_{\triangle_0} F((\xi, \eta), \mathbf{r}_{t_j}) \psi_t((\xi, \eta)) \left\| \frac{\partial \mathbf{r}}{\partial \xi} \times \frac{\partial \mathbf{r}}{\partial \eta} \right\| d\xi d\eta \\
&= \int_{\triangle_0} \hat{F}(\xi, \eta, \mathbf{r}_{t_j}) \, d\xi d\eta.
\end{aligned}
\tag{36}
$$

If $\mathbf{r}_{t_j}$ is not a vertex of the element $\triangle_t$, then the integrand $\hat{F}(\xi, \eta, \mathbf{r}_{t_j})$ has no singularity on the element $\triangle_0$ so that the Gaussian quadratures for the triangular element $\triangle_0$ can be employed to evaluate the integral I. For example,

$$
I \approx |\triangle_0| \sum_{i=1}^{6} w_i \hat{F}(\xi_i, \eta_i, \mathbf{r}_{t_j}),
\tag{37}
$$

where the weights w_i and nodes (ξ_i, η_i) are listed in the Table 1.

However, if $\mathbf{r}_{t_j}$ is a vertex of the element $\triangle_t$, then the integrand $\hat{F}(\xi, \eta, \mathbf{r}_{t_j})$ will have the singularity at the mesh vertex $(0,0), (1,0)$, or $(0,1)$ of the element $\triangle_0$. In this case, in order to evaluate the integral I, we may introduce the local polar coordinate transformation case by case to take the singularity away.

Case 1: singularity at the mesh vertex $(0,0)$ of the element $\triangle_0$, see the left Table 1

The weights w_i and nodes (ξ_i, η_i) in (37).

i	w_i	ξ_i	η_i
1	0.22338158	0.10810301	0.44594849
2	0.22338158	0.44594849	0.10810301
3	0.22338158	0.44594849	0.44594849
4	0.10995174	0.81684757	0.09157621
5	0.10995174	0.09157621	0.81684757
6	0.10995174	0.09157621	0.09157621

plot in Fig. 7. The polar coordinate transformation is taken as

$$\xi(\rho, \alpha) = \rho \cos \alpha. \qquad \eta(\rho, \alpha) = \rho \sin \alpha,$$

so that the integral I may be transformed into

$$I = \int_{\triangle_0} \hat{F}(\xi, \eta, \mathbf{r}_{t_j}) \, d\xi d\eta = \int_0^{\frac{\pi}{2}} d\alpha \int_0^{\frac{1}{\cos\alpha + \sin\alpha}} d\rho \left[\rho \hat{F}(\xi(\rho, \alpha), \eta(\rho, \alpha), \mathbf{r}_{t_j}) \right]. \tag{38}$$

Case 2: singularity at the mesh vertex $(0, 1)$ of the element $\triangle_0$, see the middle plot in Fig. 7. The polar coordinate transformation is taken as

$$\xi(\rho, \alpha) = \rho \cos \alpha, \qquad \eta(\rho, \alpha) = 1 + \rho \sin \alpha,$$

so that we have

$$I = \int_{\triangle_0} \hat{F}(\xi, \eta, \mathbf{r}_{t_j}) \, d\xi d\eta = \int_{\frac{3\pi}{2}}^{\frac{7\pi}{4}} d\alpha \int_0^{\frac{1}{\cos(\alpha - 3\pi/2)}} d\rho \left[\rho \hat{F}(\xi(\rho, \alpha), \eta(\rho, \alpha), \mathbf{r}_{t_j}) \right]. \tag{39}$$

Case 3: singularity at the mesh vertex $(1, 0)$ of the element $\triangle_0$, see the right plot in Fig. 7. The polar coordinate transformation is taken as

$$\xi(\rho, \alpha) = 1 + \rho \cos \alpha, \qquad \eta(\rho, \alpha) = \rho \sin \alpha,$$

so that we have

$$I = \int_{\triangle_0} \hat{F}(\xi, \eta, \mathbf{r}_{t_j}) \, d\xi d\eta = \int_{\frac{3\pi}{4}}^{\pi} d\alpha \int_0^{\frac{1}{\cos(\pi - \alpha)}} d\rho \left[\rho \hat{F}(\xi(\rho, \alpha), \eta(\rho, \alpha), \mathbf{r}_{t_j}) \right]. \tag{40}$$

After the above polar coordinate transformation, the integral I becomes regular and can be calculated by using the Gaussian quadratures. Specially, the above three cases can be casted into the unified form and can be calculated as follows

$$I = \int_{\alpha_d}^{\alpha_u} d\alpha \int_0^{\hat{\rho}(\alpha)} d\rho \left[\rho \hat{F}(\rho, \alpha, \mathbf{r}_{t_j}) \right] = \sum_{i=1}^{I_1} \sum_{s=1}^{S_1} w_i \rho_{i,s} \hat{F}(\rho_{i,s}, \alpha_i, \mathbf{r}_{t_j}), \tag{41}$$

where w_i denotes the product of corresponding Gaussian quadrature weight, and $\{\alpha_i, i = 1, 2, \cdots, I_1\}$ are Gaussian quadrature points within the interval
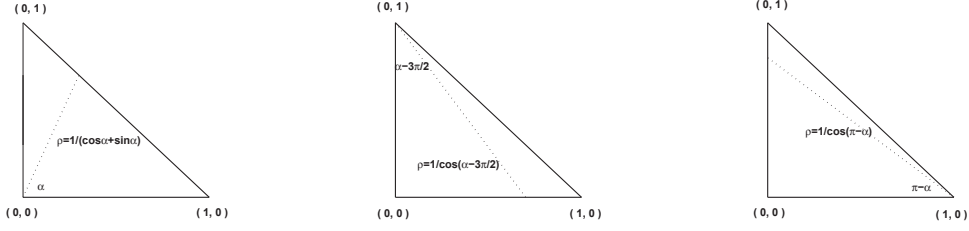
Fig. 7. left: singularity at $(0,0)$; middle: singularity at $(1,0)$; right: singularity at $(0,1)$.

(α_d, α_u), while $\{\rho_{i,s}, s = 1, 2, \cdots, S_1\}$ are Gaussian quadrature points within the interval $(0, \hat{\rho}(\alpha_i))$,

5. Image charge method for the reaction field $\phi_{\rm rf}(\mathbf{r})$

The second method we are investigating for the hybrid solvation model of ion channels (with a configuration of the finite-height cylinder) is the image charge method, which is developed in [43] to find the reaction potential $\phi_{\rm rf}(\mathbf{r})$ in (2). This section will briefly summarizes the image charge method. To derive the image charge representation of the reaction field $\phi_{\rm rf}(\mathbf{r})$, the inhomogeneity due to layered and infinite-height cylinder interfaces is considered separately, and then the results for each type of the interfaces are assembled to form the image charge method for the hybrid solvation model of ion channels.

The image charge method is based on the uniqueness theorem of the P-B equation, which allows using virtual charges to represent equivalently the reaction field as a result of the polarization field from the dielectric medium outside the cylinder. Mathematically, the solution of the P-B equation is approximated by a sum of the Coulomb potentials from a group of point charges. For a simple cavity like a sphere, such a result can be obtained analytically [8,11].

However, for a finite cylinder, the situation is more complicated.

5.1 Image charges for a layered medium

Again, consider the three-layer structure as shown in Fig. 2. The middle membrane layer with a thickness D has a low dielectric constant $\varepsilon_2 = \varepsilon_m$, typically, $\varepsilon_m = 2$. The electric potential ϕ_m in the membrane layer satisfies a Poisson equation:

$$\nabla^2 \phi_m(\mathbf{r}, \mathbf{r}_s) = -\frac{4\pi q_s}{\varepsilon_m} \delta(\mathbf{r} - \mathbf{r}_s), \tag{42}$$

where a source charge q_s is located at $\mathbf{r}_s$ (corresponding to Eq.(1) with $N = 1$) in the membrane layer and the ionic solvents in regions Ω_1 and Ω_3 are characterized by dielectric permittivities ε_1 and ε_3 and the inverse Debye-Hückel lengths λ_1 and λ_3, respectively. The potentials in these two regions are governed by the linearized P-B equation

$$\nabla^2 \phi - \lambda_i^2 \phi = 0, \quad \in \Omega_i, i = 1, 3,$$

As in (2), the potential ϕ_m inside the membrane layer can be rewritten as the sum of a Coulombic contribution $\phi_{\mathrm{coul}}(\mathbf{r}, \mathbf{r}_s) = q_s/\varepsilon_m|\mathbf{r} - \mathbf{r}_s|$ and a reaction potential ϕ_{rf} due to the polarization of the ionic solvents by the source charge q_s. By a detailed analysis using the continuous interface condition of the potential and the normal displacement at the interface, the analytical expansion of the reaction field can be found to be [43]:

$$\phi_{\mathrm{rf}}(\mathbf{r}, \mathbf{r}_s) = \int_0^{+\infty} \int_0^{+\infty} d\alpha d\beta \cos\alpha(x - x_s) \cos\beta(y - y_s)[A(\alpha, \beta)e^{\gamma z} + B(\alpha, \beta)e^{-\gamma z}], \tag{43}$$

where

$$A(\alpha, \beta) = \frac{2q_s}{\varepsilon_m \pi \gamma} \frac{e^{-\gamma(D - z_s)}(\gamma - \tau_1)(\gamma + \tau_3) + e^{-\gamma(D + z_s)}(\gamma - \tau_1)(\gamma - \tau_3)}{(\gamma + \tau_1)(\gamma + \tau_3)e^{\gamma D} - (\gamma - \tau_1)(\gamma - \tau_3)e^{-\gamma D}}, \tag{44}$$

$$B(\alpha, \beta) = \frac{2q_s}{\varepsilon_m \pi \gamma} \frac{e^{\gamma(D - z_s)}(\gamma + \tau_1)(\gamma - \tau_3) + e^{-\gamma(D - z_s)}(\gamma - \tau_1)(\gamma - \tau_3)}{(\gamma + \tau_1)(\gamma + \tau_3)e^{\gamma D} - (\gamma - \tau_1)(\gamma - \tau_3)e^{-\gamma D}}, \tag{45}$$

24

and $\gamma = \sqrt{\alpha^2 + \beta^2}$, $\tau_i = \varepsilon\sqrt{\gamma^2 + \lambda_i^2}$, $i = 1, 3$. Although the integrand in (43) is damped exponential function, numerical calculation of (43) is still time consuming. Our goal is to find some image charges such that the sum of their electrostatic potentials gives an accurate approximation to the reaction field as

$$\phi_{\text{rf}}(\mathbf{r}, \mathbf{r}_s) \approx \phi_{\text{irf}}(\mathbf{r}, \mathbf{r}_s) = \frac{1}{\varepsilon_m} \sum_{images} \frac{q_{image}}{|\mathbf{r} - \mathbf{r}_{image}|}. \tag{46}$$

In order to reach such a goal, two strategies have been proposed [43] to find out the locations and the magnitudes of the image charges.

Strategy 1: we fix the location of the kth pair of the image charges at $\mathbf{x}_{\pm k}$ due to physical symmetry,

$$\mathbf{r}_k = (x_k, y_k, z_k) = \left(x_s, y_s, (-1)^k \left(z_s - \frac{D}{2}\right) + \left(k + \frac{1}{2}\right) D\right), \quad k = \pm 1, \pm 2, \cdots. \tag{47}$$

Then by minimizing the discrete L_2 error between the image based potential field and the exact potential, we can get the magnitudes of the image charges $q_{\pm k}$.

Strategy 2: we construct the image charges using Prony approximation, where a sum of exponentials is used to approximate the Fourier transform of the exact reaction field potential (43). After applying the inverse Fourier transform to the sum of exponentials, both locations and magnitudes of the images can be obtained.

5.2 Image charges for an infinite-height cylinder

For an infinite-height cylinder of radius a, consider a point charge q_s located at position $\mathbf{r}_s$ inside the cylinder. The cylinder partitions the whole space into two regions, characterized by dielectric constants ε_0 and ε_m, respectively.

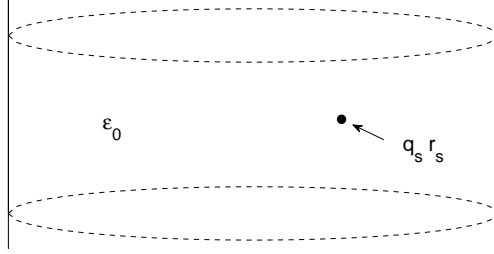According to [15] , the reaction potential of the point charge q_s at $\mathbf{r}_s =$

Fig. 8. Schematic illustration of an infinite-height cylinder.

(ρ_s, φ_s, z_s) under the cylindrical coordinate system can be approximated as

$$\phi_{\rm rf}^{\rm cylinder}(\mathbf{r}, \mathbf{r}_s) \approx \phi_{\rm irf}^{\rm cylinder}(\mathbf{r}, \mathbf{r}_s) = \frac{1}{\varepsilon_0} \sum_{c=1}^{C} \frac{f_c}{|\mathbf{r} - \mathbf{r}_c|}. \tag{48}$$

Here $\mathbf{r}_c = (\rho_c, \varphi_s + \varphi_c, z_s)$, f_c, ρ_c and φ_c can be generated by a function depending on ε_0 and ε_m [43].

5.3   Image charge method for ion channel hybrid model

Now we can combine the results of the layered medium and the infinite cylinder to handle the inhomogeneity of the ion-channel model. Assuming that the source charge q_s is at $\mathbf{r}_s = (\rho_s, \varphi_s, z_s)$ inside an infinite cylinder with a radius of the ion channel size a. The dielectric constant inside the cylinder is that of the cavity (close to 1-2) and the dielectric constant outside the cylinder is taken as that of the membrane. The cylindrical interface will require the following image charges $f_c q_s, c = 1, ..., C$, for the approximation of the reaction field potential as in (48). Now, we introduce the planar membrane/solvent interfaces at $z = 0, D$, which will generate $2K$ image charges $q_s q_k$ and $f_c q_s q_k$, $k = \pm 1, .., \pm K$, for the approximation of the reaction field as in Strategies 1 or 2 for each of the charges q_s and $f_c q_s$. Altogether, the reaction field for the ion channel model can now be approximated by the potential of $(2K+1)(C+1)-1$

26

image charges as

$$\phi_{\mathrm{rf}}(\mathbf{r}, \mathbf{r}_s) \approx \phi_{\mathrm{irf}}(\mathbf{r}, \mathbf{r}_s) = \frac{q_s}{\varepsilon_0} \sum_{c=0}^{C} \sum_{k=-K}^{K} \frac{(1 - \delta_{c0}\delta_{k0}) f_c q_k}{|\mathbf{r} - \mathbf{r}_{c,k}|}, \tag{49}$$

where $\mathbf{r}_{c,k}$ is the image charge point given in Strategies 1 or 2 [43] indexed by k in the three layered medium for the source charge located at $\mathbf{r}_c$.

6. Numerical results

This section is to investigate the numerical accuracy and efficiency in computing the layered Green's functions and the electrostatic potential for an explicit/implicit hybrid solvation model for ion channel (in the configuration of a finite-height cylinder).

6.1 Numerical computations of layered Green's functions

In practical calculations, we will need to truncate the one-dimensional integral in (14) to some finite length, which is taken to be $L = 80$ in our tests, and then subdivide the interval $[0, L]$ into 10 subintervals; on each subinterval 30 Gauss quadrature points will be used for numerical integrations. We will consider the three-layer medium in Fig. 2 with $D = 3$.

Example 1 *As in Fig. 2 but with $\varepsilon_1 = 1, \varepsilon_2 = \varepsilon_3 = 3, \lambda_1 = \lambda_2 = \lambda_3 = 0$. Take the singular source point at $\mathbf{r}' = (x', y', z') = (0, 0, 3.5)$ and the field point at $\mathbf{r} = (0.001, 0.001, z)$. The exact Green's function is also known analytically as:*

$$G_{exact}(\mathbf{r}, \mathbf{r}') = \begin{cases} \frac{1}{4\pi\varepsilon_1 |\mathbf{r} - \mathbf{r}'|} + \frac{\varepsilon_1 - \varepsilon_2}{\varepsilon_1 + \varepsilon_2} \frac{1}{4\pi\varepsilon_1 |\mathbf{r} - \mathbf{r}''|}, & \mathbf{r} \in \Omega_1, \\ \frac{2}{\varepsilon_1 + \varepsilon_2} \frac{1}{4\pi |\mathbf{r} - \mathbf{r}'|}, & \mathbf{r} \in \Omega_2 \cup \Omega_3. \end{cases} \tag{50}$$

27

Here $\mathbf{r}'' = (x', y', 2D - z')$, D is the thickness of middle layer. Comparison between the numerical and exact Green's functions and their derivatives are given in Fig. 9 with good accuracy.
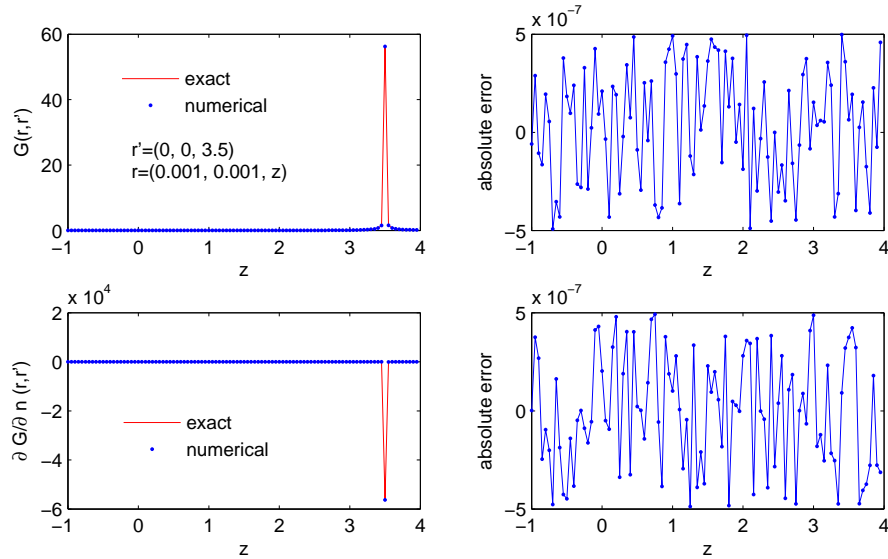

Fig. 9. Comparison of the numerical and exact Green's function, $\mathbf{n} = (1, 1, 1)$.

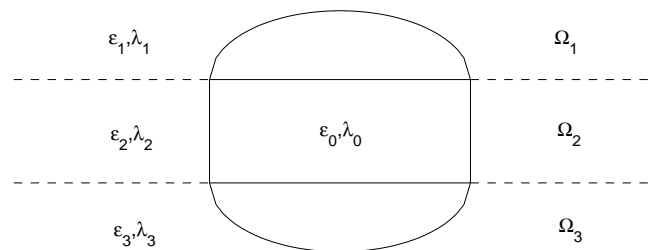*6.2 Numerical tests on the BIE method (34)*

Fig. 10. Illustration of a cylinder embedded in a three-layer structure.

Several numerical examples are presented here to validate the BIE method (34), including both homogeneous and inhomogeneous cases. As shown in Fig. 10, we consider a cylinder embedded in a three-layer structure, so the

28

Green's function obtained in Section 3 can be used. Here a $N_1 \times N_2 \times N_3$ round-top cylinder surface mesh implies that the nodes divide the radius (of z-direction) of the half sphere into N_1 equal parts, the azimuth angle into N_2 equal parts, and the height of cylinder into N_3 equal parts, respectively. For all cases, the linear system arising from the discretization of the BIE is solved by the bi-conjugate gradient method with an iteration tolerance error 10^{-10}.

Example 2 *Let $\varepsilon_1 = 1$, $\varepsilon_0 = \varepsilon_2 = \varepsilon_3 = 5$, $\lambda_0 = \lambda_1 = \lambda_2 = \lambda_3 = 0$, and the source point locates at $\mathbf{r}_s$. The exact electrostatic potential is known as*

$$
\phi(\mathbf{r}) = \begin{cases} \frac{2}{\varepsilon_1 + \varepsilon_2} \frac{q_s}{|\mathbf{r} - \mathbf{r}_s|}, & \mathbf{r} \in \Omega_1, \\[2mm] \frac{q_s}{\varepsilon_2 |\mathbf{r} - \mathbf{r}_s|} + \frac{\varepsilon_2 - \varepsilon_1}{\varepsilon_2 + \varepsilon_1} \frac{q_s}{\varepsilon_2 |\mathbf{r} - \mathbf{r}'_s|}, & \mathbf{r} \in \Omega_0 \cup \Omega_2 \cup \Omega_3, \end{cases} \tag{51}
$$

where $\mathbf{r}'_s = (x_s, y_s, 2D - z_s)$. With $q_s = 1$, the errors of the numerical results on the potential and its derivative on the cylinder surface are calculated with a $15 \times 15 \times 15$ surface mesh are shown in Fig.11.

Fig. 12 shows the error of the reaction field potential in (51) in region Ω_0 for three meshes $10 \times 10 \times 10$, $20 \times 20 \times 20$, and $40 \times 40 \times 40$, which gives a convergence rate of about 1.9.

Example 3 *In this case, we will consider a more realistic case for the hybrid model for an ion channel where $\varepsilon_0 = 1, \varepsilon_2 = 2, \varepsilon_1 = \varepsilon_3 = 80$, $\lambda_1 = 2.5, \lambda_3 = 0.5, \lambda_0 = \lambda_2 = 0$ and the radius and the height of the cylinder are $4\mathring{A}$ and $12\mathring{A}$, respectively. As an exact solution of the electrostatic potential is unavailable, we will compare with a 3D finite difference method [40] for the P-B equation with a uniform grid with a spacing $h = 0.5\mathring{A}$. The computational domain of the finite difference is taken to be $[-21\mathring{A}, 21\mathring{A}] \times [-21\mathring{A}, 21\mathring{A}] \times [-21\mathring{A}, 21\mathring{A}]$ and the boundary condition is taken approximately as given by the Coulombic potential, i.e., $\phi_{i,j,k} = q_s / \epsilon_0 |\mathbf{r}_{i,j,k} - \mathbf{r}_s|$, where $\mathbf{r}_s$ is the location of the source charge.*
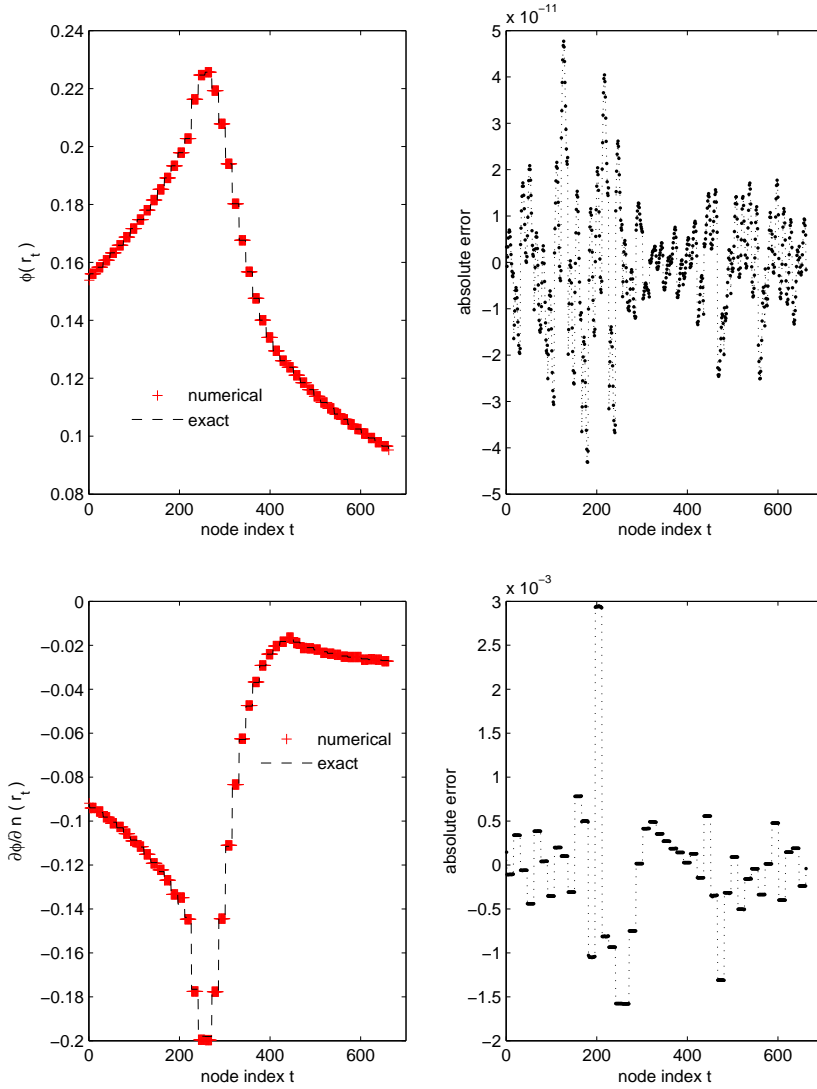
Fig. 11. Potential and its normal derivative on the boundary of a cylinder with a height of 3 and a radius of the bottom semi-sphere 1, and the source point $\mathbf{r}_s = (0, 0, 0.5)$.

The self energy $V(\mathbf{r}_s) = q_s \phi_{\mathrm{rf}}(\mathbf{r}_s)/2$ of a unit point charge $q_s = 1$ is calculated for both the boundary integral method and the finite difference method where the BIE method is implemented with a $15 \times 15 \times 15$ surface mesh; comparison of the results of both methods is given in Fig.13.

In example 2, the absolute error of the potential reaches the machine error, i.e., 10^{-11}, and the error of the normal derivative of the potential is shown to
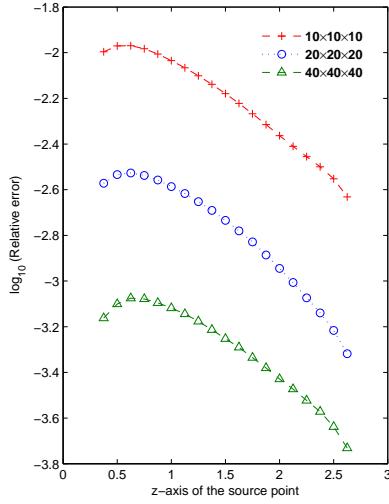
Fig. 12. error of the reaction field potential in (51) in region Ω_0
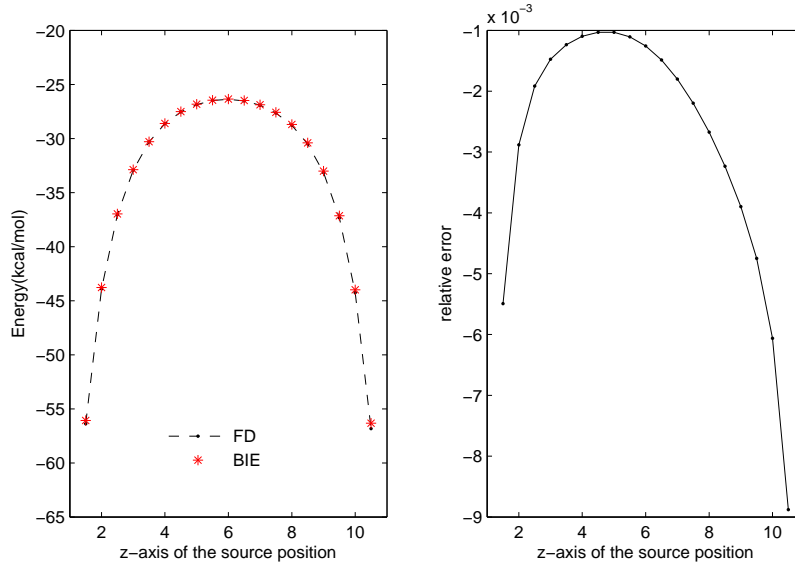
Fig. 13. The self energies and its relative errors between the boundary integral equation and the finite difference method, where the source point is $\mathbf{r}_s = (0, 0, z)$.

be around 10^{-3}. In example 3, the BIE method gives the self energy with less than 1% relative error within that of the finite difference method. However, due to the approximation to the unknown boundary data on the computational domain and the degeneracy of accuracy near the dielectric interfaces, there is uncertainty in the accuracy of the finite difference solutions. In the next

subsection, numerical convergence of the BIE method will be conducted.

6.3 Comparison of BIE and image charge method for potentials in an ion channel hybrid model

Numerical results of both the BIE and image charge methods will be given and compared in this section. First, a numerical convergence study of the BIE method will be given to validate the accuracy of the BIE method. Then, a comparison between the BIE and image charge methods will be done. We will consider the potential produced by a group of 19 source charges at $\mathbf{r}_s$ along a vertical line segment $(3, 0, z_s), 1 \leq z_s \leq 11$ inside the cylinder in Fig.1 with a radius of $4\mathring{A}$ and a height of $12\mathring{A}$ and $\varepsilon_0 = 1, \varepsilon_m = 2, \varepsilon_s = 80, \lambda_1 = 2.5$ and $\lambda_2 = 0.5$.
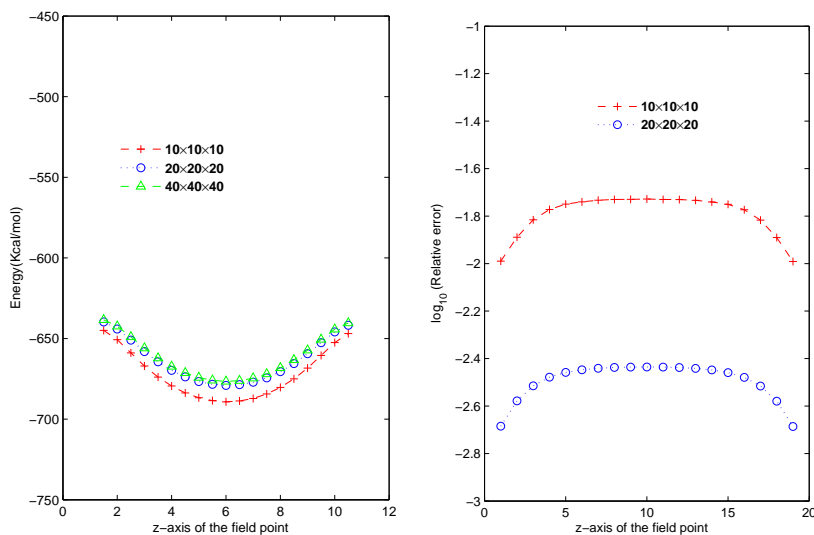

Fig. 14. Numerical convergence of potential energy from the BIE. (Left) Potential energy, (Right) error of potential energy

To study the numerical convergence rate of the BIE, we use three meshes $10 \times 10 \times 10$, $20 \times 20 \times 20$, and $40 \times 40 \times 40$ for the round-top cylinder surface, where the results obtained on the finest mesh $40 \times 40 \times 40$ is used as

the reference solution to compute the numerical convergence rate of the BIE method. In the BIE method, after the potential and its normal derivatives on the round-top cylinder surface are obtained, the potential of any point inside the cylinder can be computed through (28). Thus, we can compute the potential energy of a unit charge at $\mathbf{r}_s = (0, 0, z_s)$ defined by $V(\mathbf{r}_s) = q_s \phi_{\mathrm{rf}}(\mathbf{r}_s)/2$ where $\phi_{\mathrm{rf}}(\mathbf{r})$ is the reaction field produced by all 19 source charges. Fig. 14 contains the computed self-energy (left) and illustrates its convergence at a rate of 2.34 (right) as expected for a linear approximation for the BIE method.

With the convergence of the BIE method established, the result of the BIE method will be taken as the reference solution for the image charge method (49). The self energy $V(\mathbf{r}_s) = q_s \phi_{\mathrm{rf}}(\mathbf{r}_s)/2$ of a unit point charge located within the finite cylinder will be calculated with the image charge method with four images to treat the planar interface inhomogeneity and three images are used for the cylinder interface inhomogeneity, resulting in a 19 images for the image approximation to the reaction field (49).

We probe the accuracy of the self-energy by the two image charge methods along three different lines inside the ion-channel. Fig. 15 and Fig. 16 show the self-energy and its error relative to the $40 \times 40 \times 40$ mesh BIE result along the lines defined by $(0, 0, z)$ and $(2, 0, z)$, respectively while Fig. 17 shows the results along the line defined by $(x, 0, 2)$.

It can be seen that under 19 image charges, both image charge methods give reasonable accuracy for the reaction field in the ion channel model while the image method given by Strategy 1 has a better numerical performance than the image method given by Strategy 2, and in particular, the relative error of the former stays below 4%.

Finally, we exam the accuracy of the image charge method in terms of the number of images used, here $2K$ is the number of images used in (46) for the
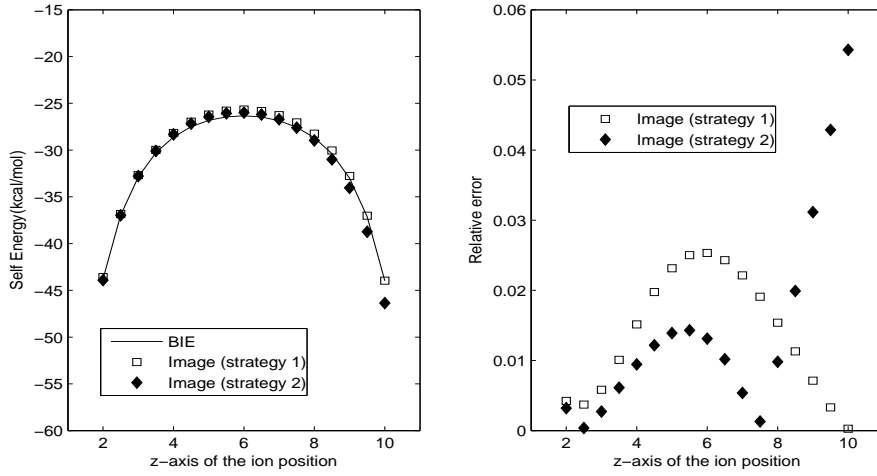
Fig. 15. The self energies and its relative errors of a unit charge located at $(0, 0, z)$ within the ion channel.
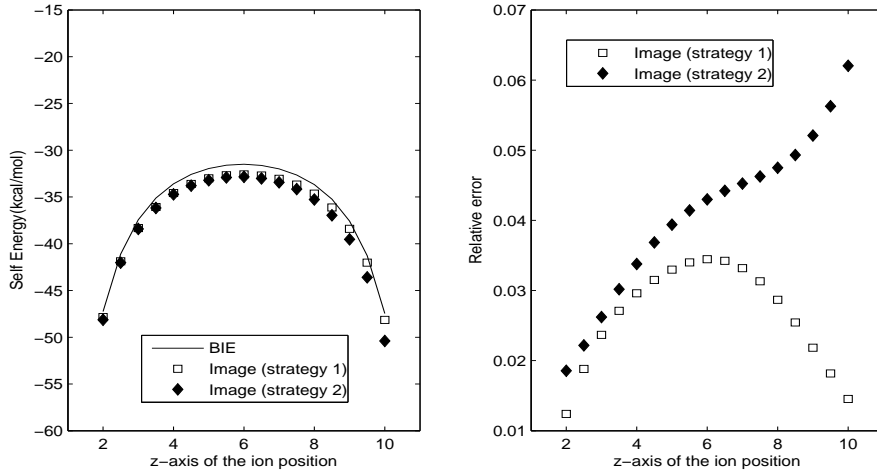

Fig. 16. The self energies and its relative errors of a unit charge located at $(2, 0, z)$ within the ion channel.

horizontal interfaces and C the number of images used in (48) for the cylindrical interface. Fig. 18 shows the decay of the error in self energy along the line $(2, 0, z)$, again measured against the results obtained by the BIE method with a $40 \times 40 \times 40$ mesh, for $(2K, C) = (4, 3)$, $(4, 4)$, and $(6, 4)$, respectively. It can be seen that the error decreases with increasing number of images for the finite-height cylinder used for the hybrid ion channel model, however, at a larger computational cost.
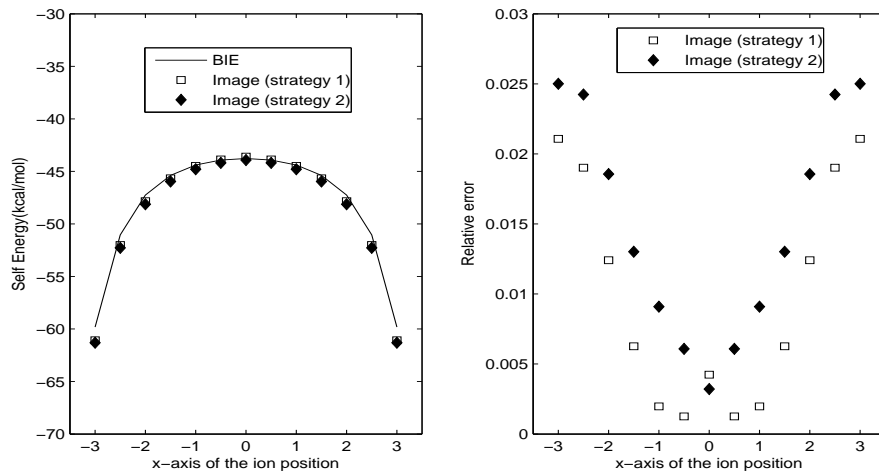
Fig. 17. The self energies and its relative errors of a unit charge located at $(x, 0, 2)$ within the ion channel.
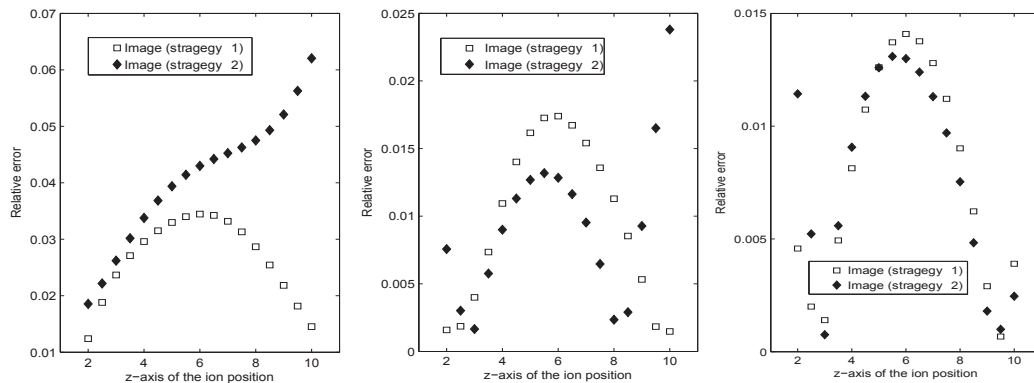

Fig. 18. Relative errors of the self energy of a unit charge located at $(2, 0, z)$ within the ion channel. left: $K = 2, C = 3$ (19 image charges), middle: $K = 2, C = 4$ (24 image charges), right: $K = 3, C = 4$ (34 image charges).

7. Conclusion

Two methods of calculating electrostatic potential in an ion channel hybrid solvation model are studied. The new boundary integral equation method avoids the edge singularity by introducing an artificial semi-sphere geometry, thus allowing a high-accuracy numerical solution serving as a benchmark reference method. The image charge method, with adjustable number of images, are

35

much less time consuming due to its inherent simplicity, have been validated by the BIE method to produce sufficient accuracy for the electrostatic potential for the hybrid model. It should be noted that as the matrix from the BIE in (34) is independent of the location of the charges inside the cylinder cavity of the hybrid model, the cost of a direct solver of the matrix equation could become less of a concern when it is pre-factorized and re-used for dynamic simulations by molecular dynamics simulations. In practical simulations, one can select either the BIE or image charge method depending on the desired accuracy and efficiency and the type of simulations.

Appendix

A   Analytical form for Green's function in a three layer medium

The Fourier spectral form of the layered Green's function $G(\mathbf{r}, \mathbf{r}')$ are given as follows.

For $\mathbf{r}' \in \Omega_1$, we have

$$
G(\mathbf{r}, \mathbf{r}') = \begin{cases} P_1(\mathbf{r}, \mathbf{r}') + \frac{1}{2\pi} \int_{-\infty}^{+\infty} \int_{-\infty}^{+\infty} dk_x dk_y e^{ik_x(x-x')} e^{ik_y(y-y')} A_1(k_\rho, z, z'), & \in \Omega_1, \\[2ex] \frac{1}{2\pi} \int_{-\infty}^{+\infty} \int_{-\infty}^{+\infty} dk_x dk_y e^{ik_x(x-x')} e^{ik_y(y-y')} \left[B_1(k_\rho, z, z') + C_1(k_\rho, z, z') \right], & \mathbf{r} \in \Omega_2, \\[2ex] \frac{1}{2\pi} \int_{-\infty}^{+\infty} \int_{-\infty}^{+\infty} dk_x dk_y e^{ik_x(x-x')} e^{ik_y(y-y')} D_1(k_\rho, z, z'), & \mathbf{r} \in \Omega_3, \end{cases}
$$

$$(A.1)$$

36

where

$$A_1(k_\rho, z, z') = e^{-\tilde{\eta}_1 z} \frac{e^{\tilde{\eta}_1(2D-z')}}{4\varepsilon_1 \tilde{\eta}_1 \pi g} \left[(\epsilon_1 \tilde{\eta}_1 + \epsilon_2 \tilde{\eta}_2)(\epsilon_2 \tilde{\eta}_2 - \epsilon_3 \tilde{\eta}_3) e^{-2\tilde{\eta}_2 D} \right.$$
$$\left. + (\epsilon_1 \tilde{\eta}_1 - \epsilon_2 \tilde{\eta}_2)(\epsilon_2 \tilde{\eta}_2 + \epsilon_3 \tilde{\eta}_3) \right],$$

$$B_1(k_\rho, z, z') = e^{-\tilde{\eta}_2 z} \frac{e^{\tilde{\eta}_1(D-z')-\tilde{\eta}_2 D}}{2\pi g} (\epsilon_2 \tilde{\eta}_2 - \epsilon_3 \tilde{\eta}_3),$$

$$C_1(k_\rho, z, z') = e^{\tilde{\eta}_2 z} \frac{e^{\tilde{\eta}_1(D-z')-\tilde{\eta}_2 D}}{2\pi g} (\epsilon_2 \tilde{\eta}_2 + \epsilon_3 \tilde{\eta}_3),$$

$$D_1(k_\rho, z, z') = e^{\tilde{\eta}_3 z} \frac{e^{\tilde{\eta}_1(D-z')-\tilde{\eta}_2 D}}{\pi g} \epsilon_2 \tilde{\eta}_2.$$

For $\mathbf{r}' \in \Omega_2$, we have

$$G(\mathbf{r}, \mathbf{r}') = \begin{cases} \frac{1}{2\pi} \int_{-\infty}^{+\infty} \int_{-\infty}^{+\infty} dk_x dk_y e^{ik_x(x-x')} e^{ik_y(y-y')} A_2(k_\rho, z, z'), & \mathbf{r} \in \Omega_1, \\[2mm] P_2(\mathbf{r}, \mathbf{r}') + \frac{1}{2\pi} \int_{-\infty}^{+\infty} \int_{-\infty}^{+\infty} dk_x dk_y e^{ik_x(x-x')} e^{ik_y(y-y')} & \mathbf{r} \in \Omega_2, \\[2mm] \qquad\qquad\qquad \cdot \left[B_2(k_\rho, z, z') + C_2(k_\rho, z, z') \right], & \\[2mm] \frac{1}{2\pi} \int_{-\infty}^{+\infty} \int_{-\infty}^{+\infty} dk_x dk_y e^{ik_x(x-x')} e^{ik_y(y-y')} D_2(k_\rho, z, z'), & \mathbf{r} \in \Omega_3, \end{cases}$$
$$\tag{A.2}$$

where

$$A_2(k_\rho, z, z') = e^{-\tilde{\eta}_1 z} \frac{e^{(\tilde{\eta}_1-\tilde{\eta}_2)D}}{2\pi g} \left[(\epsilon_2 \tilde{\eta}_2 - \epsilon_3 \tilde{\eta}_3) e^{-\tilde{\eta}_2 z'} + (\epsilon_2 \tilde{\eta}_2 + \epsilon_3 \tilde{\eta}_3) e^{\tilde{\eta}_2 z'} \right],$$

$$B_2(k_\rho, z, z') = e^{-\tilde{\eta}_2 z} \frac{e^{-\tilde{\eta}_2 z'}}{4\varepsilon_2 \tilde{\eta}_2 \pi g} (\epsilon_2 \tilde{\eta}_2 - \epsilon_3 \tilde{\eta}_3) [(\epsilon_1 \tilde{\eta}_1 + \epsilon_2 \tilde{\eta}_2) - (\epsilon_1 \tilde{\eta}_1 - \epsilon_2 \tilde{\eta}_2) e^{2\tilde{\eta}_2(z'-D)}],$$

$$C_2(k_\rho, z, z') = e^{\tilde{\eta}_2 z} \frac{e^{-2\tilde{\eta}_2 D}}{4\varepsilon_2 \tilde{\eta}_2 \pi g} (\epsilon_1 \tilde{\eta}_1 - \epsilon_2 \tilde{\eta}_2) [(\epsilon_2 \tilde{\eta}_2 - \epsilon_3 \tilde{\eta}_3) e^{-\tilde{\eta}_2 z'} + (\epsilon_2 \tilde{\eta}_2 + \epsilon_3 \tilde{\eta}_3) e^{\tilde{\eta}_2 z'}],$$

$$D_2(k_\rho, z, z') = e^{\tilde{\eta}_3 z} \frac{e^{-\tilde{\eta}_2 z'}}{2\pi g} [(\epsilon_1 \tilde{\eta}_1 + \epsilon_2 \tilde{\eta}_2) - (\epsilon_1 \tilde{\eta}_1 - \epsilon_2 \tilde{\eta}_2) e^{2\tilde{\eta}_2(z'-D)}].$$

For $\mathbf{r}' \in \Omega_3$, we have

$$
G(\mathbf{r}, \mathbf{r}') = \begin{cases}
\frac{1}{2\pi} \int_{-\infty}^{+\infty} \int_{-\infty}^{+\infty} dk_x dk_y e^{ik_x(x-x')} e^{ik_y(y-y')} A_3(k_\rho, z, z'), & \mathbf{r} \in \Omega_1, \\[2ex]
\frac{1}{2\pi} \int_{-\infty}^{+\infty} \int_{-\infty}^{+\infty} dk_x dk_y e^{ik_x(x-x')} e^{ik_y(y-y')} \left[B_3(k_\rho, z, z') + C_3(k_\rho, z, z') \right], & \mathbf{r} \in \Omega_2, \\[2ex]
P_3(\mathbf{r}, \mathbf{r}') + \frac{1}{2\pi} \int_{-\infty}^{+\infty} \int_{-\infty}^{+\infty} dk_x dk_y e^{ik_x(x-x')} e^{ik_y(y-y')} D_3(k_\rho, z, z'), & \mathbf{r} \in \Omega_3,
\end{cases}
$$
$$\text{(A.3)}$$

where

$$
\begin{aligned}
A_3(k_\rho, z, z') &= e^{-\tilde{\eta}_1 z} \frac{e^{\tilde{\eta}_1 D - \tilde{\eta}_2 D + \tilde{\eta}_3 z'}}{\pi g} \epsilon_2 \tilde{\eta}_2, \\[1ex]
B_3(k_\rho, z, z') &= e^{-\tilde{\eta}_2 z} \frac{e^{\tilde{\eta}_3 z'}}{2\pi g} (\epsilon_1 \tilde{\eta}_1 + \epsilon_2 \tilde{\eta}_2), \\[1ex]
C_3(k_\rho, z, z') &= - e^{\tilde{\eta}_2 z} \frac{e^{\tilde{\eta}_3 z' - 2\tilde{\eta}_2 D}}{2\pi g} (\epsilon_1 \tilde{\eta}_1 - \epsilon_2 \tilde{\eta}_2), \\[1ex]
D_3(k_\rho, z, z') &= e^{\tilde{\eta}_3 z} \frac{-e^{\tilde{\eta}_3 z'}}{4\varepsilon_3 \tilde{\eta}_3 \pi g} \Big[(\epsilon_1 \tilde{\eta}_1 + \epsilon_2 \tilde{\eta}_2)(\epsilon_2 \tilde{\eta}_2 - \epsilon_3 \tilde{\eta}_3) \\
&\quad + (\epsilon_1 \tilde{\eta}_1 - \epsilon_2 \tilde{\eta}_2)(\epsilon_2 \tilde{\eta}_2 + \epsilon_3 \tilde{\eta}_3) e^{-2\tilde{\eta}_2 D} \Big].
\end{aligned}
$$

In the above, the g is defined by

$$
g = (\epsilon_1 \tilde{\eta}_1 - \epsilon_2 \tilde{\eta}_2)(\epsilon_2 \tilde{\eta}_2 - \epsilon_3 \tilde{\eta}_3) e^{-2\tilde{\eta}_2 D} + (\epsilon_1 \tilde{\eta}_1 + \epsilon_2 \tilde{\eta}_2)(\epsilon_2 \tilde{\eta}_2 + \epsilon_3 \tilde{\eta}_3).
$$

B Derivation of integral equations (23) and (28)

Here we derive Eqs. (23) and (28). With the Green's second identity, the integrals on the right hand side of (22) on the boundary of $\mathbf{R}^3 \backslash (\Omega^* \cup B(\mathbf{r}', \rho))^c$ can be split into five parts, denoted by I, II, III, IV and V respectively, i.e.

$$
0 = I + II + III + IV + V,
$$

Each of them will be considered separately below.

Part I: the integral on the infinite interface.

As both $\bar{G}(\mathbf{r}, \mathbf{r}')$ and $\phi(\mathbf{r})$ vanish at infinity, $I = 0$.

Part II: the integral on the interface of the layered structure

$$II = \sum_{i=1}^{k+s} \int_{\Gamma_i^+} \left\{ \varepsilon_i \left[\bar{G}_i(\mathbf{r}, \mathbf{r}') \frac{\partial \phi_i}{\partial \mathbf{n}_i}(\mathbf{r}) - \phi_i(\mathbf{r}) \frac{\partial \bar{G}_i}{\partial \mathbf{n}_i}(\mathbf{r}, \mathbf{r}') \right] \right.$$
$$\left. - \varepsilon_{i+1} \left[\bar{G}_{i+1}(\mathbf{r}, \mathbf{r}') \frac{\partial \phi_{i+1}}{\partial \mathbf{n}_i}(\mathbf{r}) - \phi_{i+1}(\mathbf{r}) \frac{\partial \bar{G}_{i+1}}{\partial \mathbf{n}_i}(\mathbf{r}, \mathbf{r}') \right] \right\} dS(\mathbf{r})$$
$$= 0. \tag{B.1}$$

Part III: the integral on the side surface of the cylinder

$$III = - \int_{\partial \Omega_0^s} \varepsilon_{k+1} \left[\bar{G}_{k+1}(\mathbf{r}, \mathbf{r}') \frac{\partial \phi_{k+1}}{\partial \mathbf{n}}(\mathbf{r}) - \phi_{k+1}(\mathbf{r}) \frac{\partial \bar{G}_{k+1}}{\partial \mathbf{n}}(\mathbf{r}, \mathbf{r}') \right] dS(\mathbf{r}).$$

Part IV: the integral on the part of surface of the half sphere

$$IV = - \int_{P^+ \cup P^-} \bar{\varepsilon}(\mathbf{r}) \left[\bar{G}(\mathbf{r}, \mathbf{r}') \frac{\partial \phi}{\partial \mathbf{n}}(\mathbf{r}) - \phi(\mathbf{r}) \frac{\partial \bar{G}}{\partial \mathbf{n}}(\mathbf{r}, \mathbf{r}') \right] dS(\mathbf{r}).$$

Part V: the integral on $\partial B(\mathbf{r}', \rho)$

$$V = \int_{\partial B(\mathbf{r}', \rho)} \bar{\varepsilon}(\mathbf{r}) \left[\bar{G}(\mathbf{r}, \mathbf{r}') \frac{\partial \phi}{\partial \mathbf{n}}(\mathbf{r}) - \phi(\mathbf{r}) \frac{\partial \bar{G}}{\partial \mathbf{n}}(\mathbf{r}, \mathbf{r}') \right] dS(\mathbf{r})$$
$$= -\phi(\mathbf{r}'). \qquad \rho \to 0. \tag{B.2}$$

Combining $I - V$ yields (23).

Similarly, applying the Green's second identity on (27), the integral on the boundary of $\Omega^* \backslash B(\mathbf{r}', \rho)$ can be partitioned into four parts:

$$-4\pi \sum_{i=1}^{N} q_i \hat{G}(\mathbf{r}_i, \mathbf{r}') = I + II + III + IV.$$

Part I: the integral on the interface of the layered structure

$$
\begin{aligned}
I = \sum_{i=2,i\neq k,k+1}^{k+s-1} \int_{\Gamma_i^-} & \left\{ \varepsilon_i \left[\hat{G}_i(\mathbf{r},\mathbf{r}') \frac{\partial \phi_i}{\partial \mathbf{n}_i}(\mathbf{r}) - \phi_i(\mathbf{r}) \frac{\partial \hat{G}_i}{\partial \mathbf{n}_i}(\mathbf{r},\mathbf{r}') \right] \right. \\
& \left. -\varepsilon_{i+1} \left[\hat{G}_{i+1}(\mathbf{r},\mathbf{r}') \frac{\partial \phi_{i+1}}{\partial \mathbf{n}_i}(\mathbf{r}) - \phi_{i+1}(\mathbf{r}) \frac{\partial \hat{G}_{i+1}}{\partial \mathbf{n}_i}(\mathbf{r},\mathbf{r}') \right] \right\} dS(\mathbf{r}) \\
& + \int_{\Gamma_k^-} \left\{ \varepsilon_k \left[\hat{G}_k(\mathbf{r},\mathbf{r}') \frac{\partial \phi_k}{\partial \mathbf{n}_k}(\mathbf{r}) - \phi_k(\mathbf{r}) \frac{\partial \hat{G}_k}{\partial \mathbf{n}_k}(\mathbf{r},\mathbf{r}') \right] \right. \\
& \left. -\varepsilon_0 \left[\hat{G}_0(\mathbf{r},\mathbf{r}') \frac{\partial \phi_0}{\partial \mathbf{n}_k}(\mathbf{r}) - \phi_0(\mathbf{r}) \frac{\partial \hat{G}_0}{\partial \mathbf{n}_k}(\mathbf{r},\mathbf{r}') \right] \right\} dS(\mathbf{r}) \\
& + \int_{\Gamma_{k+1}^-} \left\{ \varepsilon_0 \left[\hat{G}_0(\mathbf{r},\mathbf{r}') \frac{\partial \phi_0}{\partial \mathbf{n}_{k+1}}(\mathbf{r}) - \phi_0(\mathbf{r}) \frac{\partial \hat{G}_0}{\partial \mathbf{n}_{k+1}}(\mathbf{r},\mathbf{r}') \right] \right. \\
& \left. -\varepsilon_{k+2} \left[\hat{G}_{k+2}(\mathbf{r},\mathbf{r}') \frac{\partial \phi_{k+2}}{\partial \mathbf{n}_{k+1}}(\mathbf{r}) - \phi_{k+2}(\mathbf{r}) \frac{\partial \hat{G}_{k+2}}{\partial \mathbf{n}_{k+1}}(\mathbf{r},\mathbf{r}') \right] \right\} dS(\mathbf{r}) \\
= {} & 0.
\end{aligned}
\tag{B.3}
$$

Part II: the integral on the side surface of the cylinder

$$
II = \int_{\partial \Omega_0^s} \varepsilon_0 \left[\hat{G}_0(\mathbf{r},\mathbf{r}') \frac{\partial \phi_0}{\partial \mathbf{n}}(\mathbf{r}) - \phi_0(\mathbf{r}) \frac{\partial \hat{G}_0}{\partial \mathbf{n}}(\mathbf{r},\mathbf{r}') \right] dS(\mathbf{r}).
$$

Part III: the integral on the part of surface of the half sphere

$$
III = \int_{P^+ \cup P^-} \hat{\varepsilon}(\mathbf{r}) \left[\hat{G}(\mathbf{r},\mathbf{r}') \frac{\partial \phi}{\partial \mathbf{n}}(\mathbf{r}) - \phi(\mathbf{r}) \frac{\partial \hat{G}}{\partial \mathbf{n}}(\mathbf{r},\mathbf{r}') \right] dS(\mathbf{r}).
$$

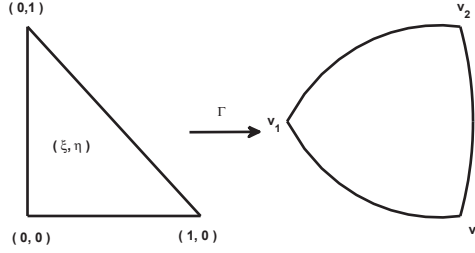**Part IV:** the integral on $\partial B(\mathbf{r}', \rho)$

$$
\begin{aligned}
IV &= \int_{\partial B(\mathbf{r}',\rho)} \hat{\varepsilon}(\mathbf{r}) \left[\hat{G}(\mathbf{r},\mathbf{r}') \frac{\partial \phi}{\partial \mathbf{n}}(\mathbf{r}) - \phi(\mathbf{r}) \frac{\partial \hat{G}}{\partial \mathbf{n}}(\mathbf{r},\mathbf{r}') \right] dS(\mathbf{r}) \\
&= -\phi(\mathbf{r}'). \qquad \rho \to 0.
\end{aligned}
\tag{B.4}
$$

Combining *I-IV* yields (28).

C The expression of mapping Γ

Here we list the specific expressions of various mappings Γ used in Eq.(36).

Case 1: The curved triangle $\triangle_t$ locates at the innermost layer of the semi-sphere surface. Denote the spherical coordinates by $(\check{r}, \check{\theta}, \check{\phi})$. The mapping Γ is defined as

$$\Gamma: \quad \mathbf{r}(\xi, \eta) = ((R\sin\check{\theta}\cos\check{\phi} + X_{center}, R\sin\check{\theta}\sin\check{\phi} + Y_{center}, R\cos\check{\theta} + Z_{center}),$$
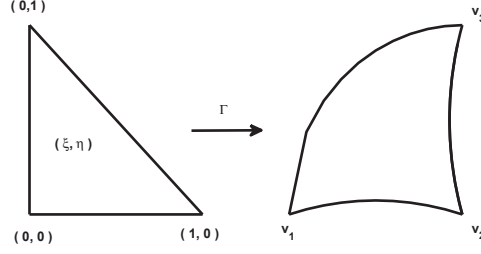$$\text{(C.1)}$$

where

$$\check{\theta} = (1 - \xi - \eta)\check{\theta}_{v_1} + (\xi + \eta)\check{\theta}_{v_2}, \qquad \check{\psi} = \begin{cases} 0, & \xi = \eta = 0, \\ \\ \frac{\eta\check{\phi}_{v_2} + \xi\check{\phi}_{v_3}}{\xi + \eta}, & \text{otherwise}, \end{cases} \qquad \text{(C.2)}$$

and the Jacobian of the mapping is

$$\left\| \frac{\partial}{\partial \xi} \times \frac{\partial}{\partial \eta} \right\| = \left| R^2 \sin(\check{\theta}) \frac{(\check{\phi}_{v_2} - \check{\phi}_{v_3})(\check{\theta}_{v_2} - \check{\theta}_{v_1})}{\xi + \eta} \right|, \qquad \text{(C.3)}$$

where R is the radius of the semi-sphere, and X_{center}, Y_{center} and Z_{center} are the coordinates of the center of the sphere.

Case 2: the curved triangle $\triangle_t$ locates on the semi-sphere surface except the innermost layer. The mapping Γ is defined as

41

$$\Gamma: \quad \mathbf{r}(\xi, \eta) = (R\sin\check{\theta}\cos\check{\phi} + X_{center}, R\sin\check{\theta}\sin\check{\phi} + Y_{center}, R\cos\check{\theta} + Z_{center}), \tag{C.4}$$

where

$$\check{\theta} = (1-\xi)\check{\theta}_{v_2} + \xi\check{\theta}_{v_3}, \qquad \check{\phi} = (1-\xi-\eta)\check{\phi}_{v_1} + (\xi+\eta)\check{\phi}_{v_3}, \tag{C.5}$$
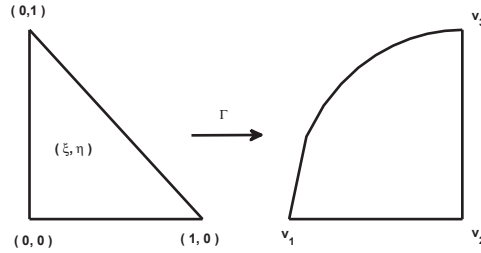
and the Jacobian of the mapping is

$$\left\|\frac{\partial}{\partial\xi} \times \frac{\partial}{\partial\eta}\right\| = \left|R^2\sin(\check{\theta})\ (\check{\phi}_{v_1} - \check{\phi}_{v_3})(\check{\theta}_{v_3} - \check{\theta}_{v_2})\right|, \tag{C.6}$$

where again R is the radius of the semi-sphere, and X_{center}, Y_{center} and Z_{center} are the coordinates of the center of the sphere.

Case 3: The curved triangle $\triangle_t$ locates on the side surface of the cylinder. Denote the cylindrical coordinate by $(\tilde{\rho}, \tilde{\theta}, \tilde{z})$. The mapping Γ is defined as

$$\Gamma: \quad \mathbf{r}(\xi, \eta) = (R\cos(\tilde{\theta}), R\sin(\tilde{\theta}), \tilde{z}), \tag{C.7}$$

where

$$\tilde{\theta} = (1-\xi-\eta)\tilde{\theta}_{v_1} + (\xi+\eta)\tilde{\theta}_{v_2}, \qquad \tilde{z} = (1-\xi)\tilde{z}_{v_1} + \xi\tilde{z}_{v_3}, \tag{C.8}$$

42

and the Jacobian of the mapping is

$$\left\| \frac{\partial}{\partial \xi} \times \frac{\partial}{\partial \eta} \right\| = \left| R \left(\tilde{z}_{v_3} - \tilde{z}_{v_1} \right) (\tilde{\theta}_{v_2} - \tilde{\theta}_{v_1}) \right|. \tag{C.9}$$

Acknowledgments

References

[1] A. Warshel, A microscopic model for calculations of chemical processes in aqueous solutions, *Chem. Phys. Lett.*, 55(1978), 454-458.

[2] G. King, A. Warshel, A surface constrained all-atom solvent model for effective simulations of polar solutions, *J. Chem. Phys.*, 91 (1989), 3647-3661.

[3] D. Beglov, B. Roux, Finite representation of an infinite bulk system: Solvent boundary potential for computer simulations, *J. Chem. Phys.*, 100(1994), 9050-9063.

[4] H. Alper, R. M. Levy, Dielectric and thermodynamic response of a generalized reaction field model for liquid state simulations, *J. Chem. Phys.*, 99(1993), 9847-9852.

[5] A. Okur, C. Simmerling, Hybrid explicit/implicit solvation methods, *Annu. Rep. Comput. Chem.*, 2(2006), 97-109.

[6] Y. Lin, A. Baumketner, S.Z. Deng, Z.L. Xu, D. Jacobs, and W. Cai, An image-based reaction field method for electrostatic interactions in molecular dynamics simulations of aqueous solutions, *J. Chem. Phys.*, 131(2009), 154103.

[7] Z.L. Xu and W. Cai, Fast analytical methods for macroscopic electrostatic models in biomolecular simulations, *SIAM Rev.*, 53(2011), 683-720.

[8] H.L. Friedman, Image approximation to the reaction field, *Mol. Phys.*, 29(1975), 1533-1543.

[9] L. Greengard and V. Rokhlin, A fast algorithm for particle simulations, *J. Comput. Phys.*, 73(1987), 325-348.

[10] L. Greengard, *The Rapid Evaluation of Potential Fields in Particle Systems*, MIT, Cambridge, 1987.

[11] W. Cai, S. Deng, D. Jacobs, Extending the fast multipole method to charges inside or outside a dielectric sphere, *J. Comput. Phys.*, 223(2007), 846-864.

[12] S.Z. Deng and W. Cai, Discrete image approximations of ionic solvent induced reaction field to charges, *Commun. Comput. Phys.*, 2(2007), 1007-1026.

[13] Z.L. Xu, S.Z. Deng, and W. Cai, Image charge approximations of reaction fields in solvents with arbitrary ionic strength, *J. Comput. Phys.*, 228(2009), 2092-2099.

[14] P. Qin, Z.L. Xu, W. Cai, and D. Jacobs, Image charge methods for a three-dielectric-layer hybrid solvation model of biomolecules, *Commun. Comput. Phys.*, 6(2009), 955-977.

[15] Z.L. Xu, W. Cai, and X. Cheng, Image charge method for reaction fields in a hybrid ion channel model, *Commun. Comput. Phys.*, 9(2011), 1056-1070.

[16] S.T. Cui, Electrostatic potential in cylindrical dielectric medium using the image charge method, *Mol. Phys.*, 104(2006), 2993-3001.

[17] G. Chandler, Galerkin's method for boundary integral equations on polygonal domains, *J. Austral. Math. Soc., Ser. B*, 26(1984), 1-13.

[18] Atkinson, K. and Graham, I. Iterative variants of the Nyström method for second kind boundary integral operators, *SIAM J. Sci. Stat. Comput.*, 13(1990), 694-722.

[19] R. A. Kress, A Nyström method for boundary integral equations in domains with corners, *Numer. Math.*, 58(1990), 145-161.

[20] J. Bremer, On the Nyström discretization of integral equations on planar curves with corners, *Appl. Comput. Harmonic Anal.*, 32(2012), 45-64.

[21] D. Boda, D. Gillespie, W. Nonner, D. Henderson, and B. Eisenberg, Computing induced charges in inhomogeneous dielectric medium: application in a Monte Carlo simulation of complex ionic systems, *Phys. Rev. E*, 69(2004), 046702.

[22] M.H. Cheng and R.D. Coalson, An accurate and efficient empirical approach for calculating the dielectric self-energy and ion-ion pair potential in continuum models of biological ion channels. *J. Phys. Chem. B*, 109(2005), 488-498.

[23] Y. Levin, Electrostatics of ions inside the nanopores and trans-membrane channels, Europhys. Lett. 76, 163 (2006)

[24] J. R. Bordin, A. Diehl, M. C. Barbosa, and Y. Levin, Ion fluxes through nanopores and transmembrane channels, Phys. Rev. E 85, 031914 (2012).

[25] W. Cai, *Computational Methods for Electromagnetic Phenomena: Electrostatics in Solvation, Scattering, and Electron Transport*, Cambridge University Press, 2013.

[26] D.G. Levitt, Modeling of ion channels, *J. Gen. Physiol.*, 113(1999), 789-794.

[27] D.P. Tieleman, P.C. Biggin, G.R. Smith, and M.S.P. Sansom, Simulation approaches to ion channel structure-function relationships, *Quart. Rev. Biophys.*, 34(2001), 473-561.

[28] B. Roux, T. Allen, S. Berneche, and W. Im, Theoretical and computational models of biological ion channels, *Quart. Rev. Biophys.*, 37(2004), 15-103.

[29] B. Hille, *Ionic Channels of Excitable Membranes*, Sinauer Associates Inc., 1992.

[30] B. Eisenberg, Crowded charges in ion channels, *Adv. Chem. Phys.*, 148(2012).

[31] P.K. Yang, S.H. Liaw, and C. Lim, Representing an infinite solvent system with a rectangular finite system using image charges, *J. Phys. Chem. B*, 106(2002), 2973-2982.

[32] J.D. Jackson, *Classical Electrodynamics*, 3rd ed., John Wiley & Sons, New York, 2001.

[33] C. Neumann, *Hydrodynamische Untersuchungen: Nebst Einem Anhange Über Die Probleme Der Elektrostatik Und Der Magnetischen Induction*, B.G. Teubner, 1883.

[34] I.V. Lindell, Application of the image concept in electromagnetism, in *The Review of Radio Science 1990-1992*, Oxford University Press, 1993, 107-126.

[35] W.T. Norris, Charge images in a dielectric sphere, *IEE Proc.: Sci. Meas. Technol.*, 142(1995), 142-150.

[36] R. Prony, Essai éxperimental et analytique: sur les lois de la dilatabilité de fluides élastique et sur celles de la force expansive de la vapeur de l'alkool, à différentes températures, *J. de l'École Polytechnique Floréal et Plairial*, 1(1795), 24-76.

[37] W.C. Chew, *Waves and Fields in Inhomogeneous Medium*, Van Nostrand Reinhold, 1990.

[38] A. Sommerfeld, *Partial Differential Equations in Physics*, Academic Press, 1949.

[39] L. Weiss, R.N. McDonough, Prony's method, z-transforms, and Padé approximation, *SIAM Rev.*, 5(1963), 145-149.

[40] W. Im, D. Beglov, and B. Roux, Continuum solvation model: computation of electrostatic forces from numerical solutions to the Poisson-Boltzmann equation, *Comput. Phys. Commun.*, 111(1998), 59-75.

[41] M.J. Rokhlin and S. Wandzura, Generalized Gaussian quadrature rules for systems of arbitrary functions, *SIAM J. Numer. Anal.*, 33(1996), 971-996.

[42] F. Fogolari, A. Brigo, and H. Molinari, The Poisson-Boltzmann equation for biomolecular electrostatics: a tool for structural biology, *J. Mol. Recognit.*, 15(2002), 377-392.

[43] H.M. Lin, Z.L. Xu, H.Z. Tang, and W. Cai, Image approximations to electrostatic potentials in layered electrolytes/dielectrics and an ion channel model. *J. Sci. Comput.*, 53(2012), 249-267.